[redacted]

7201

NRL Report 5821
Copy No. 73

UNCLASSIFIED

NRL RESEARCH AND DEVELOPMENT PROGRAM FOR THE FLEET BALLISTIC MISSILE

REPORT OF LONG RANGE RESEARCH FOR NAVY SEA-BASED DETERRENCE

[UNCLASSIFIED TITLE]

October 1, 1962

[redacted]

APPROVED FOR PUBLIC RELEASE - DISTRIBUTION UNLIMITED

DECLASSIFIED: By authority of
OPNAVINST 5570.1H 29APR88
Cite Authority Date
C. Rogers 1221.1
Entered by NRL Code

U. S. NAVAL RESEARCH LABORATORY
Washington, D.C.

[redacted]

APPROVED FOR PUBLIC RELEASE
DISTRIBUTION UNLIMITED

[redacted]

[redacted]

Previous Report in this Series

"NRL Research and Development Program for the Fleet Ballistic Missile – Report of Long Range Research for Navy Sea-Based Deterrence," NRL Report 5790 ([redacted] Report), March 1962

[redacted]

PREFACE

The various Naval laboratories, under sponsorship of the Special Projects Office, have undertaken a program of exploratory scientific investigation calculated to influence the future Navy's at-sea deterrence capability. A program of directed research of some duration is anticipated (and required) to put together elements which are fundamental to the formulation of a future sea-based deterrence weapon system concept.

An appropriate administrative framework has been established at NRL to sponsor, on a Laboratory-wide basis, the conduct of applicable exploratory research. Investigations, matched to existing NRL scientific programs and skills, have been initiated within this framework. They are broadly directed toward a consolidation of scientific knowledge and technological capabilities applicable to the initiation of a firmly scheduled development by the Navy of a sea-based deterrence weapon system matching the operational requirements of its day.

This report is one of a series intended to display the NRL research activity directed to support this follow-on, sea-based deterrence weapon system concept. The five papers included in this report are: A Graphical-Numerical Method for the Transient Response of Nonlinear Systems; Influence of Crystal Surface on the Optical Transmission of LiF in the Vacuum Ultraviolet; Small Fatigue Cracks as Fracture Origins in Tests of High-Strength Steel Sheet; Application of Fracture Mechanics to Adhesive Joints; and A New Submarine Detection System.

Peter Waterman
Staff Adviser for FBM

CONTENTS

A GRAPHICAL-NUMERICAL METHOD FOR THE TRANSIENT RESPONSE OF NONLINEAR SYSTEMS

[Unclassified]

P. F. Cunniff

The Naval Research Laboratory (Mechanics Division) has been conducting transient-response studies of nonlinear one- and two-degree-of-freedom nonautonomous systems by a graphical-numerical method, which is a modification of the general phase-plane method, in conjunction with numerical computations. Present analytical procedures are adequate for response studies of linear structures, but there is need for new and better procedures for analyzing the effects of structural nonlinearities. This is a step in the continuing problem of the evaluation of the effects on equipment, on ships or missiles, when subjected to the various shock and vibration environments where the often-nonlinear structural "feedback" effects must be recognized.

. . . . . FBM Staff

INTRODUCTION

One of the more important decisions which the engineer must make in the field of structural dynamics is the choice of model to serve as a representation of a structure subjected to dynamic forces. One model configuration, which is used herein, consists of concentrated masses connected in a straight line by weightless springs and dashpots. The behavior of the model under prescribed forcing functions, which are called inputs, provides the analyst with the dynamic characteristics of the structure; such behavior is classified as transient response, steady-state vibrations, and random vibrations. Each classification of response depends on the input to the system. In what follows, only transient response is considered.

The physical characteristics of the models as represented in the differential equations of motion can lead to either linear or nonlinear model systems. The dynamic analysis of linear elastic structures has been previously reported (1,2). For those models which have nonlinear characteristics of either mass, damping, or restoring forces, the transient solution of the differential equations of motion is usually unknown as a combination of elementary functions, and approximate techniques are resorted to. These methods are generally numerical, graphical, and electrical analog solutions. Graphical and numerical methods have been developed for single-degree-of-freedom systems and, in many instances, are applied only to autonomous systems.

It is the purpose of this report* to present a reasonably rapid, yet fairly precise, technique for the approximate transient solution of nonlinear multi-degree-of-freedom systems. The nonlinear components of the systems under study are assumed to be cubic hardening and cubic softening springs.

*A slightly more expanded form of the material contained in this report is available as NRL Report 5785, of the same title.

GRAPHICAL-NUMERICAL METHOD

General Equations of Motion

The equations of motion for the model configuration under study which consists of r concentrated masses can be reduced to

$$\ddot{x}_1 + \omega_i^2(x_i + \delta_i) = 0, \quad i = 1, 2, \ldots, r \tag{1}$$

where

$$\delta_i = \delta_i(x_{i+1}, x_i, x_{i-1}, \dot{x}_{i+1}, \dot{x}_i, \dot{x}_{i-1}, t),$$

and the dots refer to differentiation with respect to time. A graphical solution for this system can be obtained on r phase-planes by extending the phase-plane method (3) in conjunction with simple numerical computations.

Single Degree of Freedom

The phase-plane method is normally applied to nonlinear single-degree-of-freedom systems and has been extended to linear two-degree-of-freedom systems by superimposing normal coordinates (4). The differential equation of motion for a single-degree-of-freedom system might be written as

$$\ddot{x} + \omega^2(x + \delta) = 0. \tag{2}$$

A geometrical interpretation of Eq. (2) can be obtained by introducing new coordinates which are called the phase-plane coordinates. Let $x = x$ and $u = \dot{x}/\omega$. Equation (2) then reduces to the form

$$\frac{dx}{du} = -\frac{u}{x + \delta}. \tag{3}$$

The δ has the same dimension as x and may be represented along the x-axis in the phase-plane as shown in Fig. 1(a). The slope of the normal to the line PQ is $-u/(x + \delta)$. Since this slope is the same as Eq. (3), the phase trajectory at P will be normal to the direction PQ.

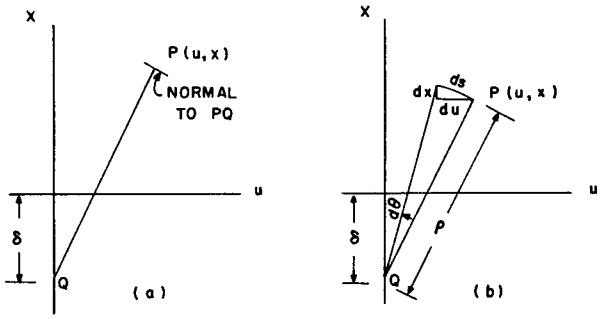

Fig. 1 - The phase-plane: (a) phase-plane coordinates representing the differential equation of motion, $\ddot{x} + \omega^2(x + \delta) = 0$, where $x = x$ and $u = \dot{x}/\omega$; (b) geometrical representation of the phase trajectory dx/du. From (a) we see that the slope of the normal to PQ is $-u/(x + \delta)$. This is also given by Eq. (3) as dx/du. Thus the phase trajectory dx/du at P is normal to the direction PQ.

Assume that δ is held at its mean value for a finite time interval Δt. Equation (3) may now be integrated and more information about the phase trajectory obtained. Rewriting Eq. (3) as

$$(x + \delta)\, dx + u\, du = 0$$

and integrating leads to

$$(x + \delta)^2 + u^2 = \text{constant} = (PQ)^2, \tag{4}$$

as can be seen in Fig. 1(a). According to Eq. (4), the instantaneous phase trajectory is a circular arc passing through P with its center at $x = -\delta$, $u = 0$, i.e., at Q.

To derive a relationship between the circular arc segment, beginning at P, and the time increment Δt, note that

$$\frac{\dot{x}}{\omega} = u,$$

and

$$dt = \frac{dx}{\omega u}. \tag{5}$$

Consider Fig. 1(b), which shows the differential geometry of the phase trajectory. Let the average radius of curvature of the step be given as $QP = \rho$. Then,

$$d\theta = \frac{ds}{\rho} = \frac{\sqrt{dx^2 + du^2}}{\sqrt{u^2 + (x + \delta)^2}}.$$

This leads to

$$d\theta = \frac{\sqrt{1 + \left(\frac{du}{dx}\right)^2}}{\sqrt{1 + \frac{(x + \delta)^2}{u^2}}} \left(\frac{dx}{u}\right) = \frac{dx}{u}$$

by means of Eq. (3). Substitution of this last equation into Eq. (5) yields

$$dt = \frac{d\theta}{\omega}.$$

Since the mean value of δ was used in the derivation, this may be written as

$$\Delta\theta = \omega\, \Delta t. \tag{6}$$

Positive time is therefore represented by a counterclockwise angular variation of the normal PQ. If a linear or nonlinear second-order ordinary differential equation is reduced to this delta form, it can be integrated graphically by construction of successive circular arc segments whose centers are located on the x-axis at various step values of $x = -\delta$. The locus of these circular arc segments is the approximate phase trajectory and, therefore, the desired solution of the differential equation.

Method of Construction

The construction procedure of the phase trajectory by the delta phase-plane method for nonautonomous single-degree-of-freedom systems is now described. As an example,

consider a simple damped oscillator with a cubic hardening spring and a prescribed foundation velocity input ($\dot{y}_o$). The equation of motion is

$$m\ddot{x} + c\dot{x} + kx + \beta x^3 = -m\ddot{y}_o.$$

This is written in the δ form as

$$\ddot{x} + \omega^2(x + \delta) = 0,$$

where

$$\delta = \gamma^2 x^3 + 2\alpha u + \frac{\ddot{y}_o}{\omega^2}.$$

The constants γ and α are given by $\gamma = \beta/m\omega^2$ and $\alpha = c/2m\omega$. Assume that the graphical solution has been extended to step n, i.e., x_n and u_n are known and x_{n+1} and u_{n+1} are desired. Using the average values of the phase coordinates during the next increment of time, the δ_n equation is

$$\delta_n = \frac{\gamma^2}{8}(x_n + x_{n+1})^3 + \alpha(u_n + u_{n+1}) + \left(\frac{\ddot{y}_o}{\omega^2}\right)_n. \tag{7}$$

Since the input is known as a function of the foundation velocity, the foundation acceleration may be approximated over the finite time interval Δt by the theorem of the mean of differential calculus. Thus,

$$(\ddot{y}_o)_n = \frac{(\dot{y}_o)_{n+1} - (\dot{y}_o)_n}{\Delta t}. \tag{8}$$

So, all terms in the right-hand side of Eq. (7) are known except x_{n+1} and u_{n+1}.

As a first trial for finding x_{n+1} and u_{n+1}, the known δ_{n-1} from the previous step of the solution might be used as the first center of arc. By laying off the prescribed circular arc $\Delta\theta = \omega\Delta t$ from the coordinate (u_n, x_n) by means of a compass and protractor, preliminary values of x_{n+1} and u_{n+1} are found quickly. Calculate the first trial value of δ_n from Eq. (7). Draw a new circular arc from (u_n, x_n) with the new center at $x = -\delta_n$ so that a new coordinate (u_{n+1}, x_{n+1}) is found. Again, use this coordinate to calculate a new δ_n. This iteration process continues until the values of δ_n converge. This completes one step of the solution.

The initial conditions for a system are known, but there is no preceding value of δ established at the beginning of a problem. To calculate a trial value of δ_o, the magnitude of the phase coordinates (u_1, x_1) at the end of the first step might be assumed or the initial values of the system might be used as the average values over the interval, or a Maclaurin expansion might be used to calculate the phase coordinate (u_1, x_1) from the initial values.

Two Degrees of Freedom

The equations of motion for a two-degree-of-freedom system are written in the δ form as follows:

$$\ddot{x}_1 + \omega_1^2(x_1 + \delta_1) = 0 \tag{9}$$

and

$$\ddot{x}_2 + \omega_2^2(x_2 + \delta_2) = 0, \tag{10}$$

where

$$\delta_1 = \delta_1(x_1, x_2, \dot{x}_1, \dot{x}_2, t)$$

and

$$\delta_2 = \delta_2(x_1, x_2, \dot{x}_1, \dot{x}_2, t).$$

For example, if the equations of motion of a linear undamped system are reduced in terms of the relative displacements, the δ expressions are

$$\delta_1 = -\frac{k_2}{k_1} x_2 + \frac{\ddot{y}_o}{\omega_1^2}$$

and

$$\delta_2 = \frac{m_2}{m_1} x_2 - \frac{\omega_1^2}{\omega_2^2} x_1.$$

The graphical integration of the coupled Eqs. (9) and (10) is obtained by extending the delta phase-plane method to two phase-planes, (u_1, x_1) and (u_2, x_2). The computational method described in the preceding section is also used. If the solution has been extended to step n, $(\delta_1)_n$ and $(\delta_2)_n$ are found for step (n+1) by using the known $(\delta_1)_{n-1}$ and $(\delta_2)_{n-1}$ as the initial centers of circular arcs. This gives trial values of $[(x_1)_{n+1}, (u_1)_{n+1}]$ and $[(x_2)_{n+1}$, and $(u_2)_{n+1}]$, which allows $(\delta_1)_n$ and $(\delta_2)_n$ to be computed. The procedure is repeated, as in the case of the single-degree-of-freedom system, until $(\delta_1)_n$ and $(\delta_2)_n$ converge to their respective values.

EQUIVALENT NUMERICAL METHOD

The differential equation of motion for a linear undamped oscillator subjected to a foundation motion is

$$\ddot{x} + \omega^2 x = -\ddot{y}_o.$$

A numerical integration technique has been developed (5) for the solution of this equation where the input is known. For a finite increment of time $\Delta t = h$, assume that the initial conditions for the (n+1) interval are x_n and u_n. The solution at the end of the interval is then

$$x_{n+1} = x_n \cos \omega h + u_n \sin \omega h - \frac{1}{\omega} \int_o^h \left[\ddot{y}_o(T)\right]_n \sin \omega(h - T)\, dT$$

and

$$u_{n+1} = -x_n \sin \omega h + u_n \cos \omega h - \frac{1}{\omega} \int_o^h \left[\ddot{y}_o(T)\right]_n \cos \omega(h - T)\, dT.$$

If the foundation acceleration is defined by Eq. (8), the approximate solution equations become

$$x_{n+1} = x_n \cos \omega h + u_n \sin \omega h - \frac{(\ddot{y}_o)_n}{\omega^2} (1 - \cos \omega h)$$

$$u_{n+1} = -x_n \sin \omega h + u_n \cos \omega h - \frac{(\ddot{y}_o)_n}{\omega^2} \sin \omega h.$$

This same approach is now used for the differential equation of motion in the standard δ form, that is, for

$$\ddot{x} + \omega^2 x = -\omega^2 \delta. \tag{11}$$

Assuming that δ is held constant during a finite time increment, the solution equations for x and u at the (n+1) interval are

$$x_{n+1} = x_n \cos \omega h + u_n \sin \omega h - \delta_n(1 - \cos \omega h) \tag{12}$$

and

$$u_{n+1} = - x_n \sin \omega h + u_n \cos \omega h - \delta_n \sin \omega h. \tag{13}$$

The first two terms on the right-hand side of Eqs. (12) and (13) are known, as well as the constant coefficients of the third term δ_n. The procedure consists in using δ_{n-1} from the previous step for δ_n in Eqs. (12) and (13). These first trial values of x_{n+1} and u_{n+1} are used to find a trial value of δ_n. Equations (12) and (13) then give new values of x_{n+1} and u_{n+1} which are used to compute a new value of δ_n. The numerical procedure continues until the values of δ_n converge.

To show that this numerical procedure is the equivalent procedure of the δ graphical construction method, rearrange Eqs. (12) and (13) in the following form:

$$x_{n+1} + \delta_n = x_n \cos \omega h + u_n \sin \omega h + \delta_n \cos \omega h \tag{14}$$

and

$$u_{n+1} = - x_n \sin \omega h + u_n \cos \omega h - \delta_n \sin \omega h. \tag{15}$$

Square each side of Eqs. (14) and (15) and add the two resulting equations. Upon simplifying, the equation reduces to

$$(x_{n+1} + \delta_n)^2 + u_{n+1}^2 = (x_n + \delta_n)^2 + u_n^2. \tag{16}$$

This is precisely the equation of a circle whose center is at $x_{n+1} = - \delta_n$, $u_{n+1} = 0$, and whose radius squared is $(x_n + \delta_n)^2 + u_n^2$. It is concluded that Eqs. (12) and (13) give the same result as the previously described graphical-numerical method without a drawing error.

If Eqs. (9) and (10) are rearranged with the δ terms on the right-hand side of the equations, the solution at the (n+1) interval is established in a similar manner as in the case of a single-degree-of-freedom system. Thus,

$$(x_1)_{n+1} = (x_1)_n \cos \omega_1 h + (u_1)_n \sin \omega_1 h - (\delta_1)_n (1 - \cos \omega_1 h),$$

$$(u_1)_{n+1} = -(x_1)_n \sin \omega_1 h + (u_1)_n \cos \omega_1 h - (\delta_1)_n \sin \omega_1 h,$$

$$(x_2)_{n+1} = (x_2)_n \cos \omega_2 h + (u_2)_n \sin \omega_2 h - (\delta_2)_n (1 - \cos \omega_2 h),$$

and

$$(u_2)_{n+1} = -(x_2)_n \sin \omega_2 h + (u_2)_n \cos \omega_2 h - (\delta_2)_n \sin \omega_2 h.$$

Once again, all terms in the right-hand side of these four equations are known, except $(\delta_1)_n$ and $(\delta_2)_n$ where

$$(\delta_1)_n = g_1 \left[(x_1)_{n+1}, (u_1)_{n+1}, (x_2)_{n+1}, (u_2)_{n+1}, t \right]$$

and

$$(\delta_2)_n = g_2 \left[(x_1)_{n+1}, (u_1)_{n+1}, (x_2)_{n+1}, (u_2)_{n+1}, t \right].$$

The same iteration process is followed for the convergence to $(\delta_1)_n$ and $(\delta_2)_n$ as in the case of δ_n in the single-degree-of-freedom system.

RESULTS

For a mechanical model which idealizes a nonlinear system under a dynamic input, it is generally important to know the relative displacements during transient motion. Example problems are presented for one- and two-degree-of-freedom systems which apply the methods developed in this report for finding the relative displacements.

The graphical-numerical method is applied to the four systems shown in Fig. 2. In each case the system is initially at rest and the input is the foundation velocity shown in Fig. 3. The time duration of the input is $t = 0.500$ second, and the solution curves for each example extend to $t = 1.000$ second.

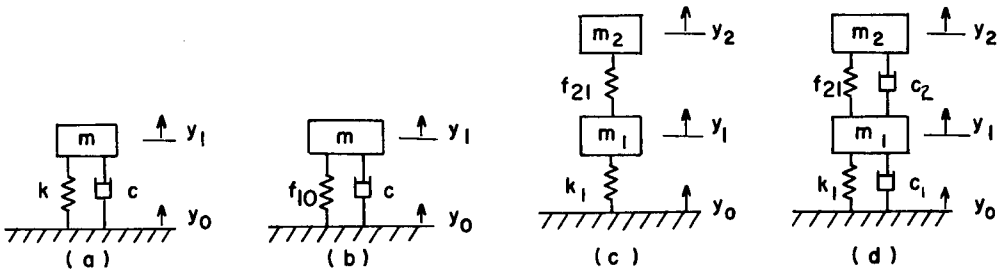

Fig. 2 - Four possible systems to which the phase-plane method is applied in this report: (a) linear, single-degree-of-freedom system with viscous damping; (b) nonlinear, single-degree-of-freedom system with both viscous damping and a cubic hardening spring; (c) nonlinear, two-degree-of-freedom system without damping and with a cubic hardening spring between m_1 and m_2; and (d) nonlinear, two-degree-of-freedom system with viscous damping and a cubic hardening spring between m_1 and m_2.

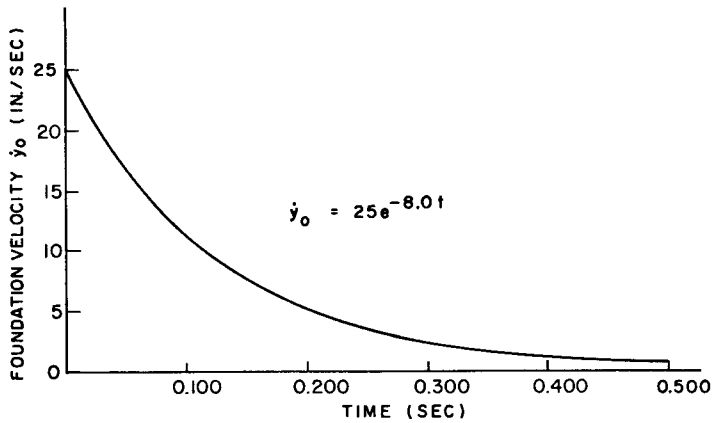

Fig. 3 - Example of a prescribed foundation velocity input $\dot{y}_o$. (The time duration of the input for this example is 0.500 sec.) For a simple damped oscillator with a cubic hardening spring and a prescribed foundation velocity input, the equation of motion is $m\ddot{x} + c\dot{x} + kx + \beta x^3 = -m\ddot{y}_o$.

The construction of the phase-plane trajectories by the graphical-numerical method is obtained by using a compass to lay off the required circular arc and a protractor to measure the angle of increment $\Delta\theta$. An engineer's scale measures the coordinate points on the phase-plane. The solutions for the nonlinear systems are compared with their respective approximate solutions on an analog computer at NRL. The computer results for each problem are in the form of plots of relative displacement x versus time t. The graphical-numerical solution and the exact solution of the linear system shown in Fig. 2(a) are presented in the Appendix and are compared with the approximate results of the analog computer for this problem (Fig. A1(b), Appendix).

The system shown in Fig. 2(b) is solved in Example 1(b) by the numerical equivalent procedure of the graphical-numerical method. This provides a check on the drawing error for this problem.

Example 1(a)

Fig. 2(b) is a model of a nonlinear single-degree-of-freedom system with viscous damping and a cubic hardening spring. The δ equation is

$$\delta = 2\alpha u + \frac{\gamma^2}{\omega^2} x^3 \frac{\ddot{y}_o}{\omega^2}.$$

The parameter values are

$$m = 0.20 \frac{\text{lb} - \text{sec}^2}{\text{in.}}; \quad k = 77.2 \frac{\text{lb}}{\text{in.}};$$

$$c = 0.75 \frac{\text{lb} - \text{sec}}{\text{in.}}; \quad \beta = 15.4 \frac{\text{lb}}{\text{in.}^3}.$$

So,

$$\delta = 0.191\, u + 0.199\, x^3 + \frac{\ddot{y}_o}{\omega^2}.$$

An increment of time $\Delta t = 0.025$ second was used throughout the solution so that $\Delta\theta = 28.13$ degrees. The δ_n equation is

$$\delta_n = 0.191 \frac{(u_n + u_{n+1})}{2} + 0.199 \frac{(x_n + x_{n+1})^3}{8} + \frac{\left[(\dot{y}_o)_{n+1} - (\dot{y}_o)_n\right]}{9.650}.$$

Since the mass is initially at rest, the initial-time coordinate conditions are

$$x_o = 0 \text{ and } u_o = -\dot{y}_o/\omega = -1.272 \text{ in.}$$

Figure 4(a) is the phase-plane trajectory composed of 40 steps in the graphical-numerical solution. As a representative step in the solution, consider the construction of the arc segment from point 6 to point 7. At the end of step 6, $x_6 = 0.391$ inch, $u_6 = 0.826$ inch, and $\delta_5 = -0.006$ inch. Use δ_5 as a first trial to find x_7 and u_7. This construction is shown in Fig. 4(b), and $x_7 = 0.737$ inch and $u_7 = 0.545$ inch. Using these values, δ_6 is calculated to be 0.026 inch. A new arc is drawn as shown in Fig. 4(b) so that $x_7 = 0.731$ inch and $u_7 = 0.532$ inch. The second value of δ_6 is 0.026 inch. Since the engineer's scale can be read to within approximately ± 0.002 inch, the construction of point 7 is complete.

Figure 4(c) is the analog computer response curve. As a comparison between the two solutions, the points plotted in Fig. 4(c) represent the x coordinates of Fig. 4(a) at 0.025-second intervals. Solution points obtained by the numerical equivalent method as presented in Example 1(b) are shown in Fig. 4(c).

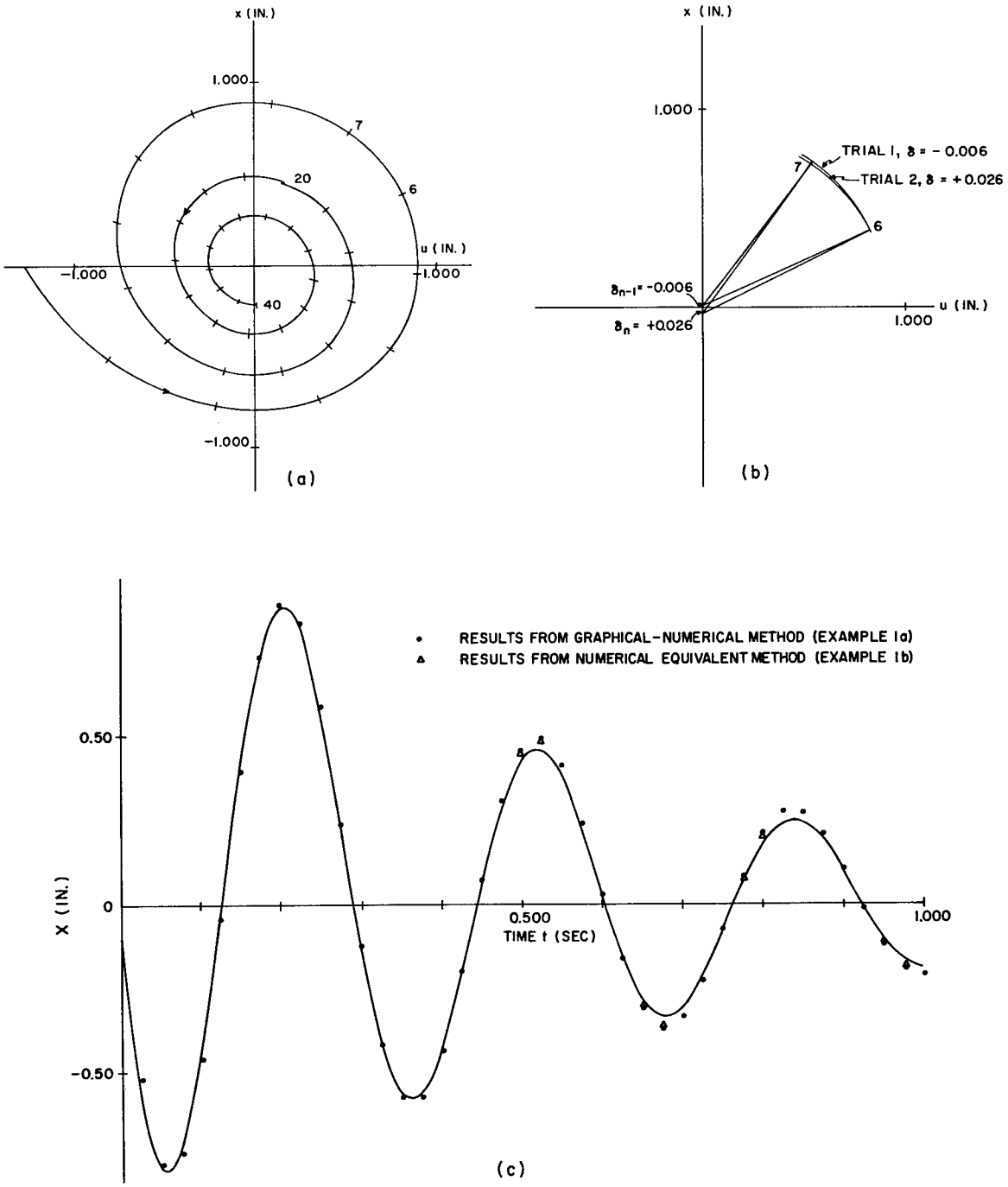

Fig. 4 - Solution of the nonlinear, single-degree-of-freedom system with viscous damping and a cubic hardening spring. (a) phase-plane trajectory consisting of 40 steps in the graphical-numerical solution with $\Delta\theta = 28.13$ degrees; (b) illustration of two trials in the evaluation of the step from (x_6, u_6) to (x_7, u_7); (c) analog-computer-approximation response curve showing values of x as functions of t. Selected results from the graphical-numerical method are shown for 0.025-second intervals as circles, the triangles representing some selected exact numerical results.

Example 1(b)

The numerical equivalent procedure of the graphical-numerical method is used to solve Example 1(a). Since $\Delta t = h = 0.025$ second throughout the problem, the solution equations are

$$x_{n+1} = 0.88178\, x_n + 0.47166\, u_n - 0.11822\, \delta_n$$

and

$$u_{n+1} = -0.47166\, x_n + 0.88178\, u_n - 0.47166\, \delta_n,$$

where

$$\delta_n = 0.09544\,(u_{n+1} + u_n) + 0.02494\,(x_{n+1} + x_n) + \frac{\left[(\dot{y}_o)_{n+1} - (\dot{y}_o)_n\right]}{9.650}.$$

The results of this method are plotted in Fig. 4(c) only where there is a noticeable difference from the values of x in Example 1(a).

Example 2

Figure 2(c) is a model of a nonlinear, two-degree-of-freedom system without damping and with a cubic hardening spring between masses m_1 and m_2. The δ equations are

$$\delta_1 = -\frac{k_2}{k_1} x_2 - \frac{\beta_2}{k_1} x_2^3 + \frac{\ddot{y}_o}{\omega_1^2}$$

and

$$\delta_2 = \frac{m_2}{m_1} x_2 + \left(\frac{1}{m_1} + \frac{1}{m_2}\right)\frac{\beta_2}{\omega_2^2} x_2^3 - \frac{\omega_1^2}{\omega_2^2} x_1.$$

The parameter values are

$$m_1 = 0.20\ \frac{\text{lb} - \text{sec}^2}{\text{in.}};\quad m_2 = 0.10\ \frac{\text{lb} - \text{sec}^2}{\text{in.}}$$

$$k_1 = 77.2\ \frac{\text{lb}}{\text{in.}};\quad k_2 = 38.6\ \frac{\text{lb}}{\text{in.}};\quad \beta_2 = 7.7\ \frac{\text{lb}}{\text{in.}^3}.$$

Hence,

$$\delta_1 = -0.500\, x_2 - 0.100\, x_2^3 + \frac{\ddot{y}_o}{\omega_1^2}$$

and

$$\delta_2 = 0.500\, x_2 + 0.299\, x_2^3 - x_1.$$

Since $\omega_1 = \omega_2 = 19.65$ rad/sec, the angle of increment is the same on each phase-plane, i.e., $\Delta\theta_1 = \Delta\theta_2 = \Delta\theta$. Figures 5(a) and 5(b) are phase trajectories for $\Delta\theta = 14.07$ degrees which required 80 steps in the solution. Figures 5(c) and 5(d) are the response curves of the analog computer. The values of $(x_1)_n$ and $(x_2)_n$ from Figs. 5(a) and 5(b) are plotted on Figs. 5(c) and 5(d) at time intervals $\Delta t = 0.025$ second as a comparison of the solutions. Response values for $\Delta\theta = 28.13$ degrees by the graphical-numerical method are also shown in the figures.

Example 3

Figure 2(d) is a model of a nonlinear two-degree-of-freedom system with viscous damping. The problem is the same as Example 2 with the addition of the damping constants, $c_1 = 0.75$ lb-sec/in. and $c_2 = 0.25$ lb-sec/in. The δ equations are

$$\delta_1 = -0.500\, x_2 - 0.100\, x_2^3 + \frac{\ddot{y}_o}{\omega_1^2} + 0.191\, u_1 - 0.064\, u_2$$

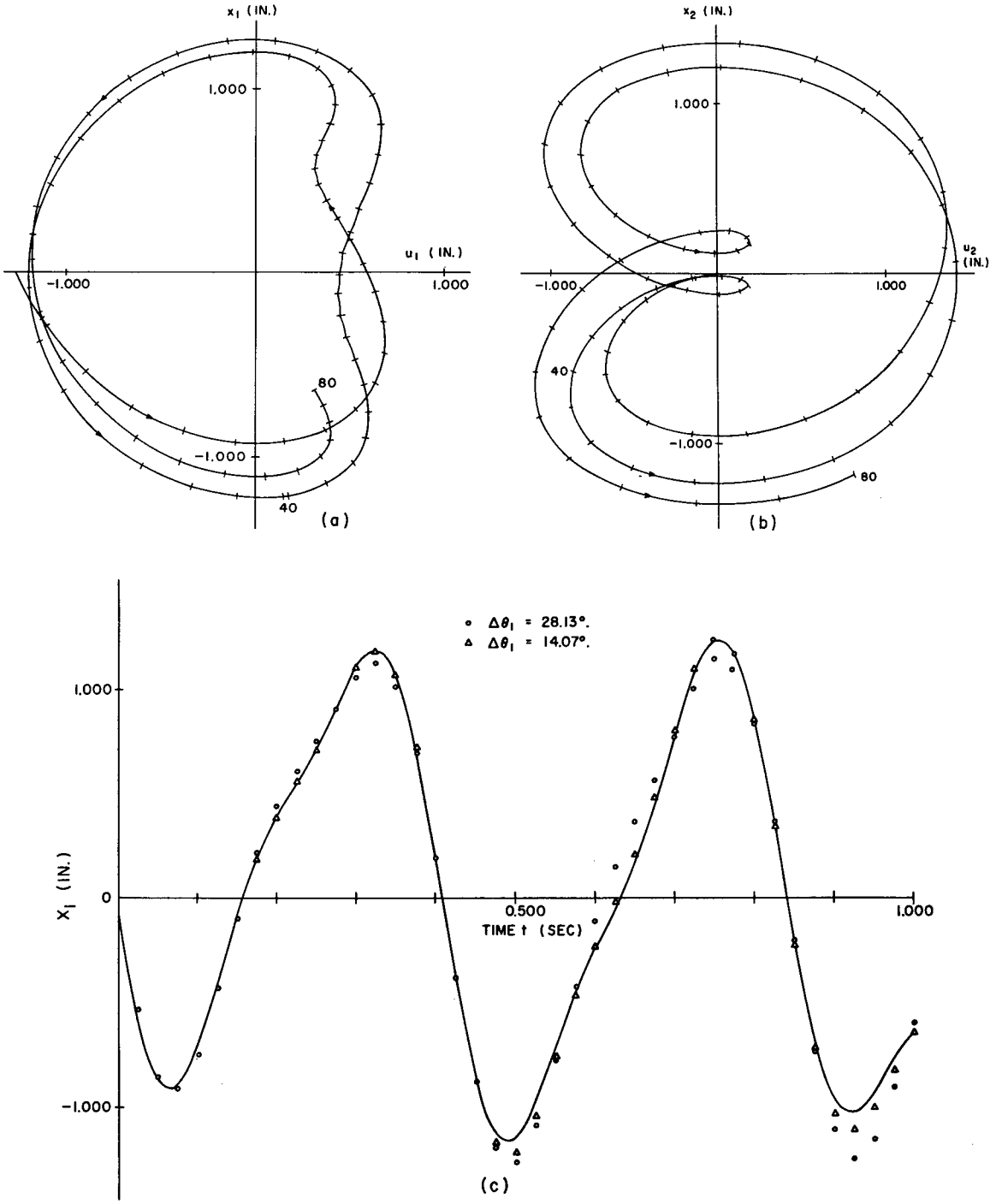

Fig. 5 - Solution of the nonlinear, two-degree-of-freedom system without damping and with a cubic hardening spring. (a) phase-plane trajectory consisting of 80 steps in the graphical numerical solution for the evaluation of x and u for m_1 with $\Delta\theta$ = 14.07 degrees; (b) the same as (a), except the values are for m_2; (c) analog-computer-approximation response curve showing values of x as functions of t; (d) the same as (c), except the curve is for values of x for the mass m_2. In (c) and (d) the circles are selected results obtained by the graphical-numerical method at 0.025-second intervals for $\Delta\theta$ = 28.13 degrees, and the triangles are some selected exact numerical results obtained for $\Delta\theta$ = 14.07 degrees.

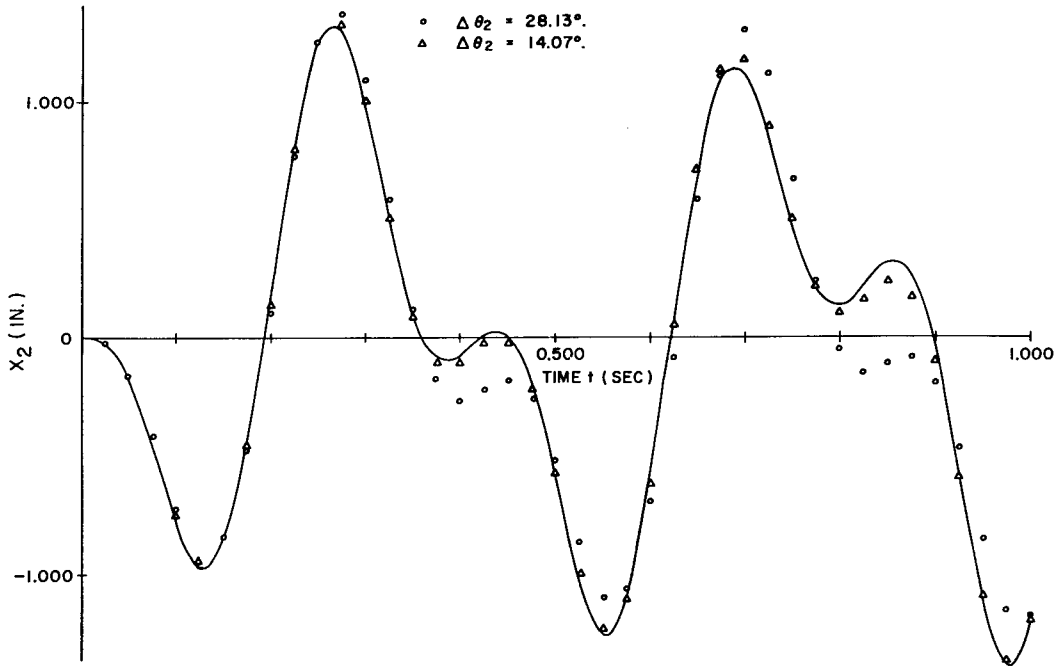

(d)

Fig. 5 (cont'd) - Solution of the nonlinear, two-degree-of-freedom system without damping and with a cubic hardening spring. (a) phase-plane trajectory consisting of 80 steps in the graphical numerical solution for the evaluation of x and u for m_1 with $\Delta\theta$ = 14.07 degrees; (b) the same as (a), except the values are for m_2; (c) analog-computer-approximation response curve showing values of x as functions of t; (d) the same as (c), except the curve is for values of x for the mass m_2. In (c) and (d) the circles are selected results obtained by the graphical-numerical method at 0.025-second intervals for $\Delta\theta$ = 28.13 degrees, and the triangles are some selected exact numerical results obtained for $\Delta\theta$ = 14.07 degrees.

and

$$\delta_2 = 0.500\, x_2 + 0.299\, x_2^3 - x_1 + 0.191\, u_2 - 0.191\, u_1.$$

Figures 6(a) and 6(b) are the graphical solutions consisting of 80 steps at $\Delta\theta$ = 14.07 degrees, while Figs. 6(c) and 6(d), are the solution curves obtained from the analog computer. The values of $(x_1)_n$ and $(x_2)_n$ from Figs. 6(a) and 6(b) are plotted at time intervals Δt = 0.025 second on Figs. 6(c) and 6(d) for comparison of the solutions. Response values for $\Delta\theta$ = 28.13 degrees by the graphical-numerical method are also shown in the figures.

DISCUSSION

The construction of the phase-plane trajectories by the graphical-numerical method required a protractor, an engineer's scale, a set of triangles, and a compass, while a desk calculator was used for computing the numerical values of the δ's. A scale of 1 inch = 0.400 inch was selected for each phase-plane coordinate system so that the investigator was able to read a coordinate to within 0.002 inch. (The construction of a circular

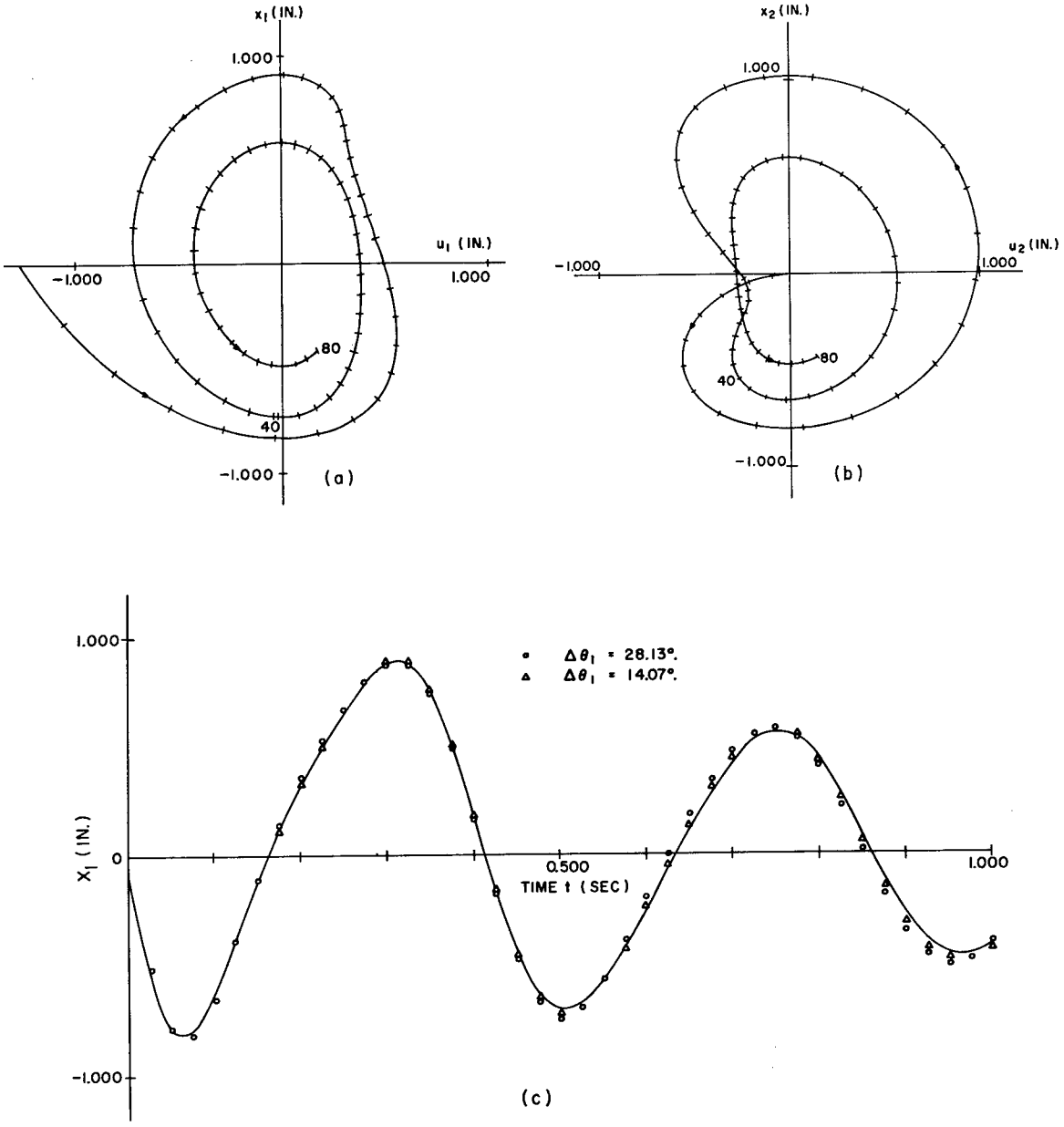

Fig. 6 - Solution of the nonlinear, two-degree-of-freedom system with viscous damping and a cubic hardening spring. (a) phase-plane trajectory consisting of 80 steps in the graphical-numerical solution for the evaluation of x and u for m_1 with $\Delta\theta$ = 14.07 degrees; (b) the same as (a), except the values are for m_2; (c) analog-computer-approximation response curve showing values of x as functions of t; (d) the same as (c), except the curve is for values of x for mass m_2. In (c) and (d) the circles are selected results obtained by the graphical-numerical method at 0.025-second intervals for $\Delta\theta$ = 28.13 degrees, and the triangles are some selected exact numerical results obtained for $\Delta\theta$ = 14.07 degrees.

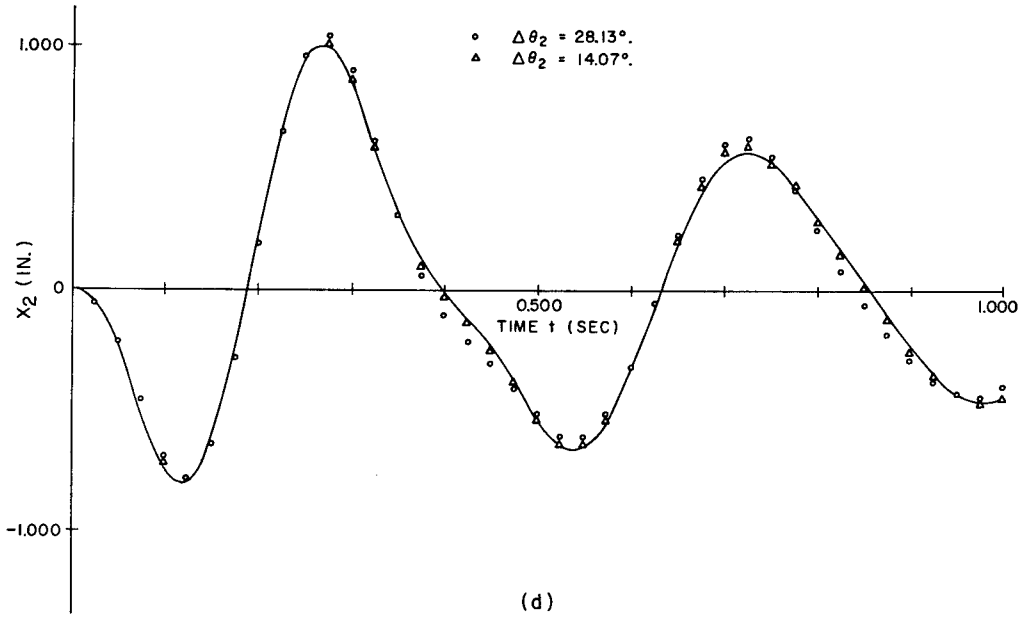

Fig. 6 (cont'd) - Solution of the nonlinear, two-degree-of-freedom system with viscous damping and a cubic hardening spring. (a) phase-plane trajectory consisting of 80 steps in the graphical-numerical solution for the evaluation of x and u for m_1 with $\Delta\theta$ = 14.07 degrees; (b) the same as (a), except the values are for m_2; (c) analog-computer-approximation response curve showing values of x as functions of t; (d) the same as (c), except the curve is for values of x for mass m_2. In (c) and (d) the circles are selected results obtained by the graphical-numerical method at 0.025-second intervals for $\Delta\theta$ = 28.13 degrees, and the triangles are some selected exact numerical results obtained for $\Delta\theta$ = 14.07 degrees.

arc segment for each step required that the trial values of the δ's converge to within ±0.002 inch.) The protractor which measured the angle of increment $\Delta\theta$ is calibrated to 0.5 degree. It appears that an angle can be read approximately to within 0.2 degree.

The example of a linear single-degree-of-freedom system in the Appendix serves two purposes. The exact values of x are compared with the results of the graphical-numerical method (Fig. A1(a)) and the analog computer (Fig. A1(b)). This provides a check on the accuracy of the analog computer. The values of relative displacement using the graphical-numerical method are plotted at increments of 0.025 second on Fig. A1(b). The exact values of x are computed at intervals of 0.050 second and are plotted on the figure where there is a noticeable difference from the graphical-numerical results. The greatest differences between the exact solution and the computer curve occur at t = 0.500 second and t = 0.750 second; this difference is approximately 0.033 inch. Otherwise, the values compare quite favorably.

The results of the nonlinear systems of Examples 1, 2, and 3 are shown in Figs. 4, 5, and 6. In each case the graphical-numerical results agree favorably with the analog computer curves. The iteration process for each example generally required two trials in each step for the δ's to converge to within ±0.002 inch.

The numerical equivalent procedure was used in Example 1(b) to find the drawing error in the graphical-numerical method applied to the system of Example 1(a). The results show that the two methods are in agreement, as seen in Fig. 4(c).

CONCLUSIONS

If the equations of motion for a nonlinear system are reduced to the standard delta form, as in Examples 1(a), 2, and 3, the graphical-numerical method is readily adaptable for finding the approximate displacement for a given transient input. For nonautonomous systems whose input is in the form of a foundation velocity, the corresponding foundation acceleration at finite increments of time can be approximated by the theorem of the mean of differential calculus. The graphical-numerical method is straightforward to apply, and the time required to solve a problem depends upon the number of variable terms in the δ equation and the degree of accuracy desired. From the experience gained in the example problems, the proposed technique of using δ_{n-1} from the previous step as the first trial of δ_n has been useful for obtaining a rapid convergence of δ_n. The following listing shows the approximate time required for one person to solve each of the first three examples.

Example	Angular Increment (deg)	Steps	Time (hr)
1(a)	28.13	40	6-1/2
2	14.07	80	16
3	14.07	80	20

The numerical equivalent procedure is applied with the aid of a desk calculator. This procedure has shown that the drawing error of the graphical-numerical method can be quite small, as indicated in Example 1(b). For problems where a high degree of accuracy is required, one might first draw the phase trajectories for one or two large constant angular increments as a preliminary approach to the solution. With this information, the numerical procedure for a small angular increment could be applied to find a more accurate solution. The preliminary graphical trajectories will show where the solution curves have sharp changes of curvature and small radii of curvature. At such regions, the angular increment of the numerical solution might be further reduced in magnitude for greater accuracy.

ACKNOWLEDGMENTS

The author expresses his gratitude to D. Frederick, Professor of Engineering Mechanics, Virginia Polytechnic Institute, for his helpful criticism of this work and to G. J. O'Hara, Mechanics Division, for his beneficial suggestions.

The author acknowledges W. P. DeWitt and his staff for the analog computer solutions.

APPENDIX

SOLUTION OF LINEAR, SINGLE-DEGREE-OF-FREEDOM SYSTEM

Figure 2(a) is a model of a linear, single-degree-of-freedom system with viscous damping. The δ equation for this system is

$$\delta = 2\alpha u + \frac{\ddot{y}_o}{\omega^2}.$$

The parameter values are

$$mg = 60 \text{ lbs}; \; k = 60 \text{ lb/in.}; \; c = 0.3 \frac{\text{lb - sec}}{\text{in.}}.$$

A constant increment of time, $\Delta t = 0.025$ second, was used so that the angle of arc is $\Delta\theta \doteq 28.13$ degrees for each step of the solution. Since the mass is initially at rest, the initial-time coordinate conditions are

$$x_o = 0 \text{ and } u_o = -\dot{y}_o/\omega = -1.272 \text{ in.}$$

Figure A1(a) is the phase-plane trajectory composed of 40 steps in the graphical-numerical solution, while Fig. A1(b) is the response solution from the analog computer. The mathematical solution for this linear problem in terms of the foundation velocity is

$$x = x(o)\, e^{-\alpha\omega t} \cos pt + \frac{e^{-\alpha\omega t}}{p} \left[\alpha\omega x(o) + \dot{x}(o)\right] \sin pt$$

$$+ \frac{\dot{y}_o(o)}{p} e^{-\alpha\omega t} \sin pt + \int_o^t \dot{y}_o(T)\, e^{-\alpha\omega(t-T)} \left[\frac{\alpha\omega}{p} \sin p(t-T) - \cos p(t-T)\right] dT.$$

Values of x at time increments of 0.050 second were calculated with this equation and are plotted on Fig. A1(b) where there is a noticeable difference from the values of the graphical-numerical method.

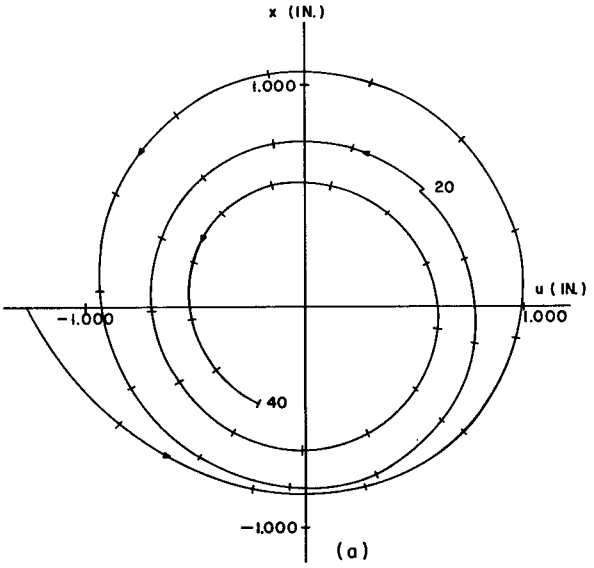

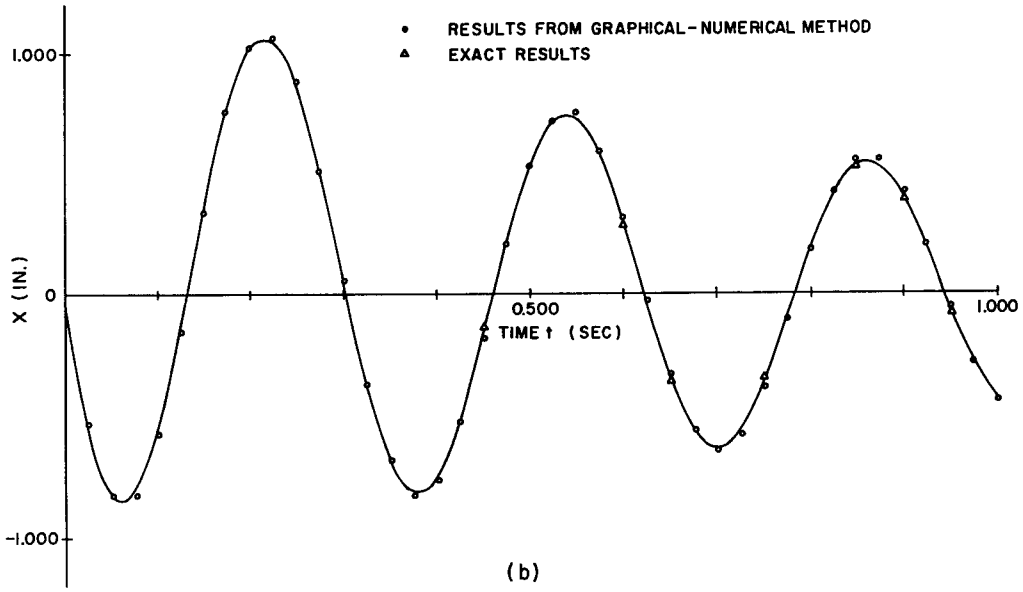

Fig. A1 - Solution of the linear, single-degree-of-freedom system with viscous damping. (a) phase-plane trajectory consisting of 40 steps in the graphical-numerical solution with $\Delta\theta$ = 28.13 degrees; (b) analog-computer-approximation response curve showing values of x as functions of t. The circles on (b) represent selected results obtained by the graphical-numerical method for $\Delta\theta$ = 28.13 degrees and for 0.025-second intervals, and the triangles are some selected exact numerical results for 0.050-second intervals.

SYMBOLS

c_i - viscous damping constant between m_i and m_{i-1}

f_{10} - nonlinear spring force between m and the foundation: $k_1 x_1 + \beta_1 x_1^3$

f_{21} - nonlinear spring force between m_2 and m_1: $k_2 x_2 + \beta_2 x_2^3$

h - finite time increment: Δt

k_i - spring constant between m_i and m_{i-1}

m_i - ith mass

p - $\omega\sqrt{1 - \alpha^2}$

t - independent time variable

u_i - scaled system velocity: $\dot{x}_i / \omega_i$

x_i - relative displacement between m_i and m_{i-1}

y_i - absolute displacement of m_i

y_o - absolute displacement of the foundation

α_i - $c_i / (2 m_i \omega_i)$

β_i - coefficient of nonlinear term of spring

γ_i^2 - β_i / m_i

δ_i - phase-plane delta for the ith equation of motion

$\Delta\theta$ - angular increment of circular arc of the phase-plane

ω_i^2 - k_i / m_i

REFERENCES

1. Blake, R.E., and Swick, E.S., "Dynamics of Linear Elastic Structures," NRL Report 4420, Oct. 1954

2. O'Hara, G.J., "Notes on Dynamics of Linear Structures," NRL Report 5387, Oct. 1959

3. Jacobsen, L.S., "On a General Method of Solving Second-Order Ordinary Differential Equations by Phase-Plane Displacements," J. Appl. Mech. 19:543 (1952)

4. Ayre, R.S., "Transient Vibration of Linear Multi-Degree-of-Freedom Systems by the Phase-Plane Method," J. Franklin Inst. 253:153 (1952)

5. O'Hara, G.J., "A Numerical Procedure for Shock and Fourier Analysis," NRL Report 5772, June 1962

INFLUENCE OF CRYSTAL SURFACE ON THE OPTICAL TRANSMISSION OF LiF IN THE VACUUM ULTRAVIOLET [Unclassified]

D. A. Patterson and W. H. Vaughan

The Naval Research Laboratory (Solid State Division) has been concerned with the study of imperfections and the effects of imperfections on the properties of solids. These studies have emphasized optical, etch, and x-ray techniques for gross imperfections. A sensitive light scattering apparatus has been built and is being used to study impurities in the alkali halides. A second very useful technique is a sensitive hardness test which has been used to study the motion of dislocations. The materials being investigated include a variety of water-soluble crystals ranging from simple cubic alkali halides, both pure and containing various additives, and complex structures such as ammonium phosphate.

. . . . . FBM Staff

INTRODUCTION

The optical properties of lithium fluoride single crystals have been studied for more than fifty years, most recently by Kato (1) et al. Since these crystals are transparent farther into the vacuum ultraviolet (to about 1050A) than any other material, they have found a great many uses in that spectral region as windows for light sources and detectors, substrates for study of thin films, and as prisms and lenses. Since the vacuum ultraviolet transmission of LiF is substantially reduced by mechanical polishing, thin optical plates are usually obtained by cleavage. Hence, the mechanical properties of the crystal have an important effect on the ease with which optical plates are obtainable.

Some LiF crystals recently received from the Harshaw Chemical Company have been found to be much more difficult to cleave, and the present investigation started out simply to improve the cleavage properties by addition of divalent impurities, cleaving at low temperature, exposure to ionizing radiation, or by some combination of the three. However, inconsistencies in the optical transmission measurements on successive days had to be accounted for and became the principal subject of this paper.

EXPERIMENTAL

The optical measurements in the vacuum ultraviolet were made using a half-meter grating spectrometer of the Seya-Namioka type manufactured by the McPherson Instrument Corporation. The light source was a dc discharge with hydrogen flowing continuously through the capillary into the vacuum chamber. Optical transmission values were computed at the peaks of strong lines to minimize corrections.

Samples from a number of different LiF crystals were studied, but those with which the data in this paper were obtained are all from the same block unless otherwise stated. They were sliced from $2 \times 1/2 \times 1/2$ inch crystal, purchased in 1958 from Harshaw Chemical Company, which cleaved very easily into good, thin plates. The samples varied in thickness from 0.20 to 0.125 cm, with little difference being observed either in initial

properties or in subsequent behavior. They were mounted with dots of light vacuum grease on six-position slides which could be translated into the light beam for measurement.

High-humidity exposures were made in a small (48 cu in.) plastic box half filled with water above which the sample slide was supported. Low-humidity exposures were made in a desiccator containing P_2O_5. These will be referred to as the "wet" and "dry" boxes, respectively. Vacuum treatments were done in a vacuum desiccator (without desiccant) with a liquid nitrogen cold trap in the pump line. Pressures in the vacuum treatments were 10^{-6} mm Hg, or less, and will be referred to as "good" vacuum.

RESULTS

The vacuum ultraviolet transmission of all the LiF crystals studied has been found to decrease after cleavage. In Fig. 1, curve (a) shows the transmission spectrum of a typical crystal immediately after cleavage. The same crystal 97 days later, shown in curve (b), has suffered a fairly general loss in transmission below 160 mμ. This loss does not appear to be associated with the growth of any specific absorption band, such as that due to OH^- shown, for example, in curve (c) in a different crystal.

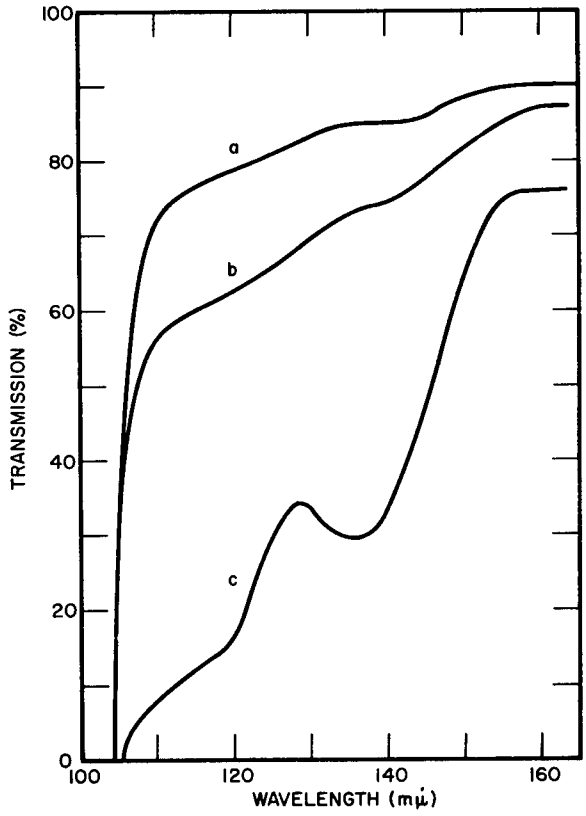

Fig. 1 - Optical transmission of LiF: (a) freshly cleaved crystal; (b) the same crystal after 97 days in air; and (c) another crystal, showing OH^- absorption band at 136 mμ (1360A).

Since no specific absorption bands appeared as the transmission decreased, the strong hydrogen Lyman-α line at 1216A was chosen as a convenient point at which to follow the decrease as a function of time and treatment. Figure 2 shows a typical curve of transmission (at 1216A) versus time in air. The apparent "saturation" (in this case beyond about 270 hours) is characteristic. The "saturation level" is different for crystals of different origin, being sometimes as low as 50 percent of the initial transmission, but is the same for sections from any given crystal.

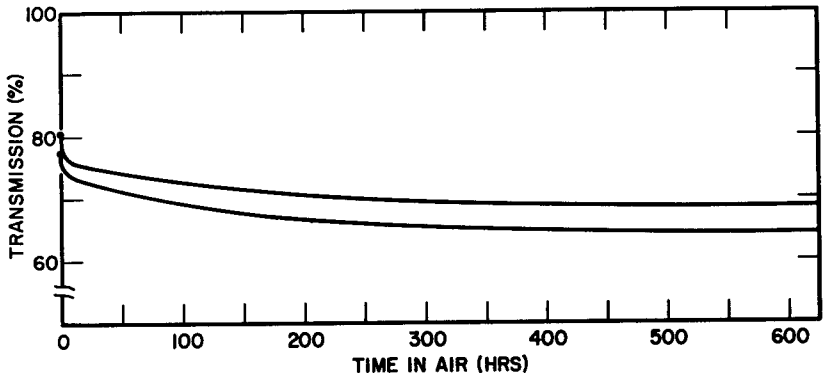

Fig. 2 - Typical curves of LiF optical transmission at 121.6mμ (the strong hydrogen Lyman-α line) versus time in air. Crystals were cleaved in dry argon gas.

Two general effects suggest themselves as possible causes of the observed decrease in transmission: (a) crystal defects, such as a post-cleavage surface relaxation of the type considered by Lennard-Jones and Dent (2), or the formation of a space charge layer due to differing energies of formation of positive and negative ion vacancies as calculated by Lehovec (3), or (b) a surface layer produced by adsorption or chemical reaction.

The possibility that imperfections were responsible was examined in the following manner: Two crystals, cleaved from the same cube, were chemically polished (4) after one had been mechanically polished to produce in it a dislocation density many orders of magnitude higher than in its mate. Both crystals showed essentially the same transmission and decay behavior. The surface relaxation mechanism was discarded because the decay was not independent of environment, as is shown later. Thus, it was concluded that mechanical defects were probably not responsible.

Since mechanical defects did not seem to be the cause, the surface layer possibility was investigated. Moisture is a common enemy of the alkali halides, and LiF, despite its relatively low solubility, is apparently no exception. This is demonstrated in Fig. 3 which shows the effect on two crystals which were exposed to room air for 250 hours and then transferred to the wet box. The high-humidity exposure clearly accelerated the transmission loss. The "saturation level," however, is the same as that of the crystals exposed to room air (Fig. 2) despite continued wet-box exposure to 600 hours.

Additional data on this moisture effect are shown in Fig. 4 for two thin crystals simultaneously cleaved in air. One was measured immediately as a control and, as curve (a) shows, was quite characteristic in its initially high transmission, decay curve (out to 200 hours) and approach to the "saturation level" at 85 percent of the initial value.* The rest of curve (a) will be discussed in a later section. The other crystal was stored 55 days in the dry box before being measured. The results of subsequent air exposure are shown in curve (b). The step discontinuities are due to vacuum treatments, discussed later. If the crystals were truly identical, then a loss of about 6 percent of the initial transmission occurred during storage. If the 85 percent saturation level characteristic of the parent

*All crystals from this block, unless given a heat treatment or chemical polish, eventually decayed to 85 percent of the initial transmission.

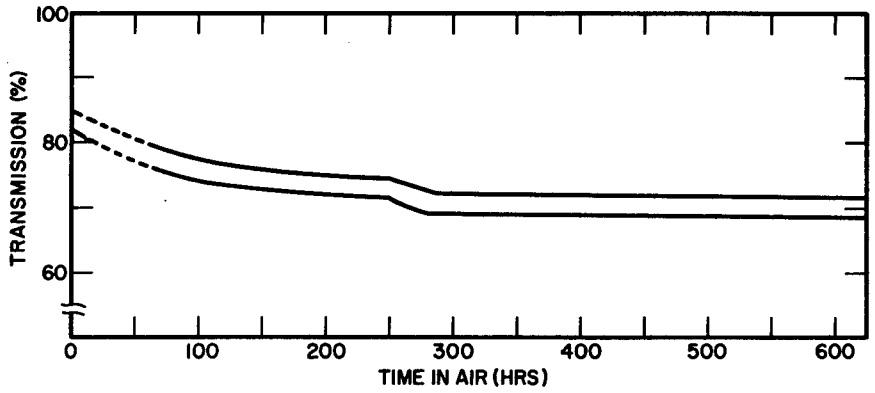

Fig. 3 - Optical transmission at 121.6 mμ versus time in air. Transfer from room air to high-humidity air at 250 hours caused more rapid decrease to "saturation level." Crystals were cleaved in air.

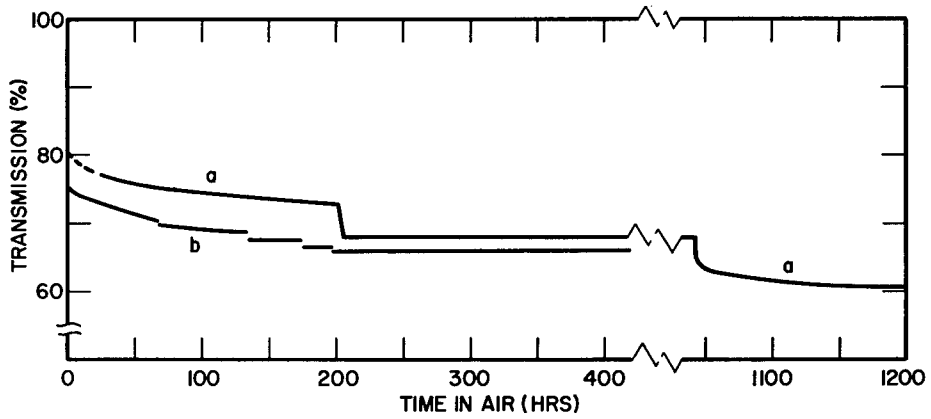

Fig. 4 - Optical transmission at 121.6 mμ versus time in air. (a) at 200 hours, a 20-hour "good" vacuum exposure dropped the transmission to "saturation." Five more days of "good" vacuum had no effect. At 1042 hours, 3 hours of "good" vacuum at 500°C caused further decrease. (b) effects of "good" vacuum exposures of 2 to 6 hours are shown at 70, 135, 175, and 195 hours. Crystals were cleaved in air.

crystal block is assumed for curve (b), then about 3 percent loss has occurred. Thus, a relative transmission loss of less than 6 percent in 55 days in dry air as compared to 15 percent in less than 15 days in room air indicates that the transmission decay is very substantially inhibited by dry-air storage.

The further step of replacing air by an inert gas was also examined. Two crystals were cleaved in dry argon and stored there for 46 days before the data in Fig. 5 were taken. The control curves are provided by Fig. 2 for which the crystals were cleaved at the same time in the same conditions. Comparison of initial values shows that again only a small decrease of around 3 percent could have occurred during the storage.* Thus, it concluded that moisture is the principal offender, that the cleavage atmosphere has no permanent effect since both crystals decay in essentially the same way when exposed to room air, and that physical changes, such as surface stress relaxation after cleavage, are not responsible.

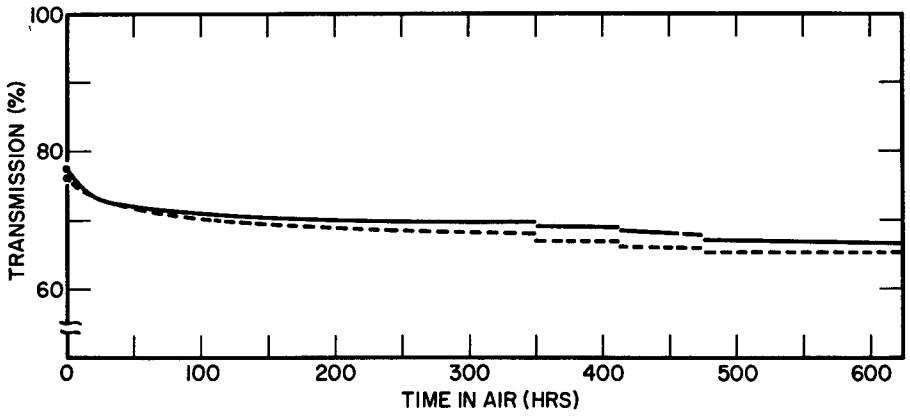

Fig. 5 - Optical transmission at 121.6 mμ versus time in air for two LiF crystals cleaved and stored in dry argon gas for 46 days before measurements. Comparison with control curves of Fig. 2 indicates less than 5 percent loss of relative transmission during storage.

Since this is a surface effect primarily dependent on the atmosphere, the possibility of an adsorbed layer which might be removed by reducing the ambient pressure was tested. It was consistently observed that the transmission of samples stored in the monochromator ($P < 5\mu$) did not change. In Fig. 2, for example, the first 7-2/3 hours of air exposure actually occurred over an 8-day period in segments of roughly 1 hour each. These air exposures were separated by periods of 24 hours or more in the monochromator during which no change occurred. Storage in a "good" vacuum also usually had no effect. However, prominent exceptions to this were observed, an example of which is shown in Fig. 4, curve (a), at 200 hours. At this point, 20 hours in a "good" vacuum decreased the transmission to the 85 percent "saturation level." Continued pumping for a total of 5 days

*This uncertainty arises from the fact that the initial transmissions of two plates cleaved from the same block can differ by 3 percent. This is probably caused by variations in the amount of plastic bending and the density of tear markings.

caused no further change. This saturation, plus the lack of change in five other saturated crystals simultaneously exposed, eliminated oil deposition as a cause. Smaller decreases after periods of 2 to 6 hours in "good" vacuum are also shown in Fig. 4, curve (b), and in Fig. 5.

In order to check this vacuum-induced decrease, a fresh crystal, cleaved in air, was subjected alternately to periods of 0.5 to 7 hours of a wet-box exposure and of 3 to 40 hours in a "good" vacuum. The accelerating effect of the wet box was again observed, and the "good" vacuum exposures had no effect until after 43 hours total wet-box exposure (30 days after cleavage). At this point the vacuum-induced decrease was observed, dropping from 88 to 85 percent in 2 hours and then to 82 percent in 100 hours. Subsequent wet-box exposures had no further effect.

An explanation of this apparently anomalous behavior in vacuum may lie in a simple consideration of the reaction kinetics involved. Consider the hydrolysis reaction as occurring in two different phases distinguished by the factors determining the reaction rate. In the first phase the rate is governed by the amount of water present, with the reaction occurring essentially instantaneously at the clean crystal surface. During this phase, storage in dry gas or vacuum halts the reaction simply by removing the water. As the reaction proceeds, a film of reaction products builds up on the crystal surface. Incident water molecules must now diffuse through the film before reaction can occur, and HF must diffuse out again to maintain stoichiometry. The vacuum-induced decrease occurs during this second, diffusion-controlled phase as a result of more rapid removal of HF. Thus, exposure to gaseous HF during this phase might be expected to inhibit the decrease in transmission or even restore some of the loss.

The addition of heat during the vacuum exposure had the effect shown in the last section of curve (a), Fig. 4. At about 1042 hours the "saturated" crystal was heated (500°C for 3 hours) in "good" vacuum. Its transmission was unaffected by the treatment itself but dropped rapidly during subsequent air exposure. The similarity of this curve to those of freshly cleaved crystals (Fig. 2) might be interpreted as being due to similar crystal surface, except for its substantially lower value.

Several attempts were made to observe the forward scattering of light from surface roughening, which would contribute to the decreasing transmission, and also to see if all regions of the crystal contribute equally to the diminution in transmission. The crystal was mounted in the spectrometer light beam with an ultraviolet-sensitive photographic film close behind it. A number of crystals were thus "photographed" immediately after being cleaved and after aging, but no changes due to scattering were detected. The most striking feature of the films was the clear appearance of the surface tear markings as seen in Fig. 6. A careful study of these markings revealed no signs of broadening with age which might be expected to occur preferentially at surface steps if the surface were being attacked. The observed effect was an overall diminution in the transmission of the crystal with no increase in the background to indicate scattering of light.

This result may be justified from a knowledge of the rate of decrease in transmission and from light scattering results. Consider the simple case in which spheres of material of a differing index of refraction form on the surface. The turbidity coefficient τ describes the fractional reduction in intensity of a light beam in passing through a medium. It has been shown (5) that for scattering particles much smaller than the wavelength of light, the turbidity is proportional to the sixth power of the particle radius,

$$\tau \propto N R^6$$

and

$$\frac{d\tau}{dt} \propto 6N \frac{dR}{dt} R^5$$

Fig. 6 - A transmission photograph of a cleaved LiF crystal made with 1216A light. The tear markings on both crystal surfaces are clearly visible.

where R = radius of particle, N = number of particles per unit area, and t = time. Thus in order that the observed rate of change of transmission be attributable to light scattering, it would be necessary that dR/dt decrease at least as fast as R^{-5}, a result which seems unlikely. For example, a constant rate of increase in sphere volume would only make dR/dt vary as R^{-2}.

It is also possible that the decreased transmission is caused by very broad or overlapping absorption bands so that a specific band is not seen. Such a surface film can be expected to show interference effects with the first maximum or minimum occurring for a film thickness of $\lambda/4n$ where λ is the wavelength of the incident light (1216A), and n is the index of refraction of the film. Since no maximum or minimum was observed in the transmission as a function of time, an upper limit could be placed upon the film thickness if the surface index of refraction could be measured. Such a change in index of refraction would not be detected by the usual method of passing light through a prism and measuring the deviation. However, the relative contributions of interference and absorption to the changing transmission could be determined by reflection measurements, since an interference loss in the forward direction would show up as increased reflection in the backward direction.

Since permanent prevention and/or removal of the offending surface effect seemed difficult by atmosphere control, the possibility of modifying the crystal itself to inhibit the effect was briefly examined. Divalent impurities are known to improve the cleavage properties (6) and the optical transmission (7) of other alkali halide crystals, both of which are desirable effects. Hence, a crystal of LiF:Mg was grown* by using random pieces of high-purity LiF from Harshaw Chemical Company as raw material, with increasing amounts of MgF_2 added at regular intervals. The resulting crystal cleaved quite easily but showed reduced transmission in all sections and this approach was not pressed further.

An evaporated layer of MgF_2 has been found to protect metal mirror surfaces (8) and this approach was also tried on the crystals. A layer of MgF_2 about 40A thick was evaporated onto each surface of several crystals. This layer caused an immediate drop in transmission to about 80 percent of the precoating value (at 1216A). The transmission continued to decrease with air exposure at a more rapid rate than an uncoated crystal

*The crystal was grown at NRL by Mr. William Zimmerman, formerly of the Crystals Branch, Solid State Division.

and in 70 hours had reached 50 percent of the precoating value and was still going down. These results indicate that MgF_2 overcoating is detrimental to the optical transmission of LiF crystals in the vacuum ultraviolet.

Thin plates of LiF can be successfully cleaved at liquid nitrogen temperature, but this is an awkward process and must be done carefully to avoid extensive plastic deformation during the thermal cycle. A more convenient technique is to harden the crystal by x-radiation. A marked increase in ease of cleavage was obtained by a 1-hour x-ray exposure (225 kv, 10 ma, tungsten target). The effects of the exposure were annealed out by heating the crystals (500°C, dry argon, two hours) leaving no detectable absorption bands in the ultraviolet from 3000A to 1050A. A similar result has been recently reported by Nadeau and Johnston (9) who found that an exposure of 1.6×10^6 roentgens at room temperature made it possible to cleave the new "soft" LiF and that the radiation damage, including the absorption bands at 445 mμ and 242 mμ, could be removed by a two-hour anneal at 450°C. Their results have been confirmed in this investigation and extended to show that no radiation-induced absorption remains in the ultraviolet from 3000A to 1050A after annealing.

SUMMARY

It has been found that a general decrease in transmission below 1600A occurs when freshly cleaved LiF crystals are exposed to room air. The rate and amount of the decrease vary with crystal origin. In the crystals reported herein (all from the same block), a total decrease at 1216A of about 15 percent of the initial transmission value was essentially complete in about 10 days.

The principal cause of the decrease is a surface film apparently created by chemical reaction with moisture. The reaction can be inhibited by early storage of the crystal in dry gas or in vacuum. After some loss has occurred however, it is accelerated by vacuum storage. The transmission loss can be partially restored by chemical removal of the surface layer.

It was found that cleavage plates suitable for use as optical elements in the vacuum ultraviolet can be prepared by exposure of the new "soft" LiF to ionizing irradiation, followed by annealing in an inert gas which removes the radiation-induced absorption.

REFERENCES

1. Kato, R., et al., J. Phys. Soc. Japan 15:2111 (1960)

2. Lennard-Jones, J.E., and Dent, B.M., Trans. Faraday Soc. 24:92 (1928)

3. Lehovec, K., J. Chem. Phys. 21:1123 (1953)

4. Gilman, J.J., and Johnston, W.G., GE Report No. 57-R1-1662, Jan. 1957

5. Jobst, G., Ann. Physik 78:157 (1925); La Mer, V.K., J. Phys. and Colloid Chem. 52:65 (1948)

6. Rolfe, J., Phys. Rev. Letters 1:56 (1958); Pretzel, F.E., et al., J. Phys. Chem. Solids 16:10 (1960)

7. Etzel, H.W., and Patterson, D.A., Phys. Rev 112:1112 (1958)

8. Hass, G., and Tousey, R., J. Opt. Soc. Am. 49:593 (1959)

9. Nadeau, J.S., and Johnston, W.G., J. Appl. Phys. 32(No. 12)2563, Dec. 1961

SMALL FATIGUE CRACKS AS FRACTURE ORIGINS IN TESTS OF HIGH-STRENGTH STEEL SHEET
[Unclassified]

J. E. Srawley

The Naval Research Laboratory (Metallurgy Division) is investigating the crack propagation resistance of high-strength steels and comparable materials for use in highly stressed structures. Specimens are provided with cracks and tested in tension to determine the dependence of tensile strength upon crack dimensions or the ability to endure repeated yield stress loading, and the results are interpreted in terms of fracture mechanics.

Methods were developed for forming small semielliptical surface cracks of controlled location and dimensions in tensile specimens by electrolytic cracking or by fatigue stressing at low nominal stress levels. The exploitations of these experimental methods for the evaluation of steels proposed for construction of advanced rocket motor casings will complement other methods of evaluation to insure that high-strength steels do have acceptable crack propagation resistance at yield strength levels of 260,000 psi and higher.
. . . . . FBM Staff

INTRODUCTION

The degree of ability to tolerate small cracks is an important factor in the efficient utilization of high-strength materials stressed in tension. The ASTM Special Committee on Fracture Testing of High Strength Materials has the responsibility of considering methods of evaluating materials in this respect and has issued two reports which may be consulted for general guidance (1,2). Some additional information is to be found in a more recent publication by Irwin and Srawley (3). The usual type of specimen employed for crack propagation testing of high-strength sheet materials is provided either with very sharp edge notches or with a central, transverse slot with very sharp ends. It has been found that slots with fatigue cracks at the ends are most effective. Another type of specimen which has been found to be of value is provided with a small surface crack, extending only partway through the thickness, rather than with a slot with cracked ends. In a previous publication, tests of specimens in which the cracks were formed by hydrogen embrittlement cracking were discussed (4). It was shown that the results were in good agreement with a relationship proposed by Irwin for simielliptical surface cracks (5) and could be used for the calculation of values of the plane-strain crack toughness K_{Ic}.

Fatigue cracking offers an alternative method of introducing small surface cracks into sheet specimens which has certain advantages over hydrogen embrittlement cracking or stress corrosion cracking. The possible effects of residual hydrogen or corrodent on the results of the subsequent tests are eliminated, and also the fatigue cracking procedure is more convenient to perform and control. However, the effective sharpness of a fatigue crack may depend upon the conditions of its formation. Plastic deformation of the material in the vicinity of the crack front occurs during fatigue stressing, the extent of the plastically deformed region being greater the higher the ratio of the maximum nominal stress to the yield strength of the material. Because of the many complicating factors, there is,

at present, no way of predicting just how the fatigue stressing conditions will affect the effective sharpness of the fatigue crack. It is therefore necessary to make experimental studies which will provide some guidance about this.

MATERIAL AND HEAT TREATMENT

The specimens were obtained from a single sheet of consumable electrode vacuum-melted steel of a modified AISI-SAE H-11-type tool steel composition. The sheet was nominally 1/16 inch thick and contained 0.41% C, 0.35% Mn, 0.012% P, 0.007% S, 0.91% Si, 4.81% Cr, 1.42% Mo, and 0.56% V. The specimens were 1.000 inch wide and 8.0 inches long, the lengths being in the rolling direction of the sheet.

The specimens were heat treated after machining to size and prior to fatigue cracking. All the specimens were heat treated in one batch, together with two standard sheet tensile specimens. The heat treatment was as follows: Austenitize in argon at 1850±25°F for 30 minutes, then air cool individually; temper at 1000±10°F for 2 hours and air cool; finally, the temper treatment is repeated twice. This heat treatment resulted in an ultimate tensile strength of 263,000 psi, a yield strength of 213,000 psi, and an elongation on 2-inch gage length of 6 percent. From previous tests of this material it was known that the crack toughness would be low in this condition. This relatively brittle condition was selected because it has been predicted by Irwin that sensitivity to crack sharpness in a crack propagation test should be higher the more brittle the material and the higher its yield strength (3).

FATIGUE CRACKING

A schematic diagram of the fatigue cracking arrangement is shown in Fig. 1. The specimen is clamped as a cantilever and the free end is deflected by a cam rotating at 1750 rpm. The lower support tapers to a point, as indicated in Fig. 1, which introduces an indeterminate stress concentration at the position on the specimen at which the crack is to be formed. This feature allows the location of the crack to be controlled and lowers the value of the ratio of maximum bending moment to section modulus required to develop a crack in a practical length of time. Credit for the idea is due to Yen and Pendleberry (6). With this arrangement it is possible to develop fatigue cracks without additional stress concentration. However, it was found that cracks would be initiated much more rapidly if small, sharp indentations were made in the specimens, as indicated in Fig. 1. These indentations were made with a hardened tool steel punch prior to heat treatment of the specimens.

The general relationship between the time elapsed before carcks were observed at the ends of an indentation and the length of the indentations was established in earlier work (7) and is illustrated in Fig. 2. These data apply to a different steel from the one used in the present work, but the two steels had almost the same yield strength. On the basis of Fig. 2 an indentation length of 0.05 inch was selected for the specimens for the present work. These were intended to have fatigue crack lengths of about 0.10 inch in every case. The fracture of a typical specimen is shown in Fig. 3, and it can be seen that the indentation covers only a small part of the area of the fatigue crack.

For the arrangement shown in Fig. 1 the ratio of bending moment to section modulus is given by $6Eyh/(4A^2 + 3LA)$, where E is Young's modulus, y is the deflection, h is the specimen thickness, and A and L are the dimensions indicated on Fig. 1. This is equal to 230,000y psi for the constant values of E, h, A, and L that applied to the present work. Three sets of ten specimens each were fatigue cracked using cams which applied maximum deflections of 0.263, 0.363, and 0.563 inch, respectively. The minimum deflections were zero in each case. Thus, the maximum nominal stresses for the three sets were 60,500, 83,500, and 130,000 psi.

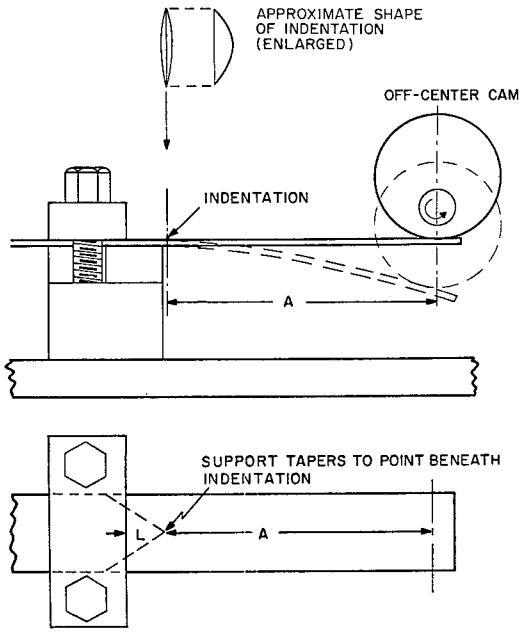

Fig. 1 - Schematic of fatigue cracking arrangement

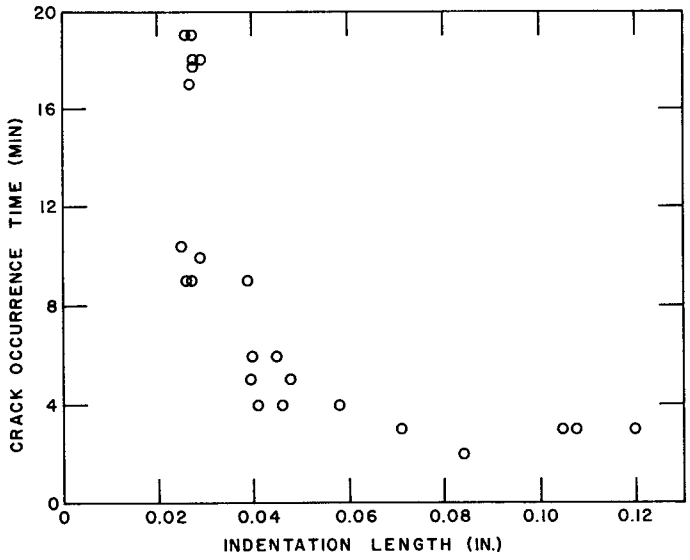

Fig. 2 - Relationship between time elapsed before formation of cracks at the ends of the indentations and indentation length for a high-strength steel. These data are for a steel different from the one used in the present investigation, but the two steels had very similar yield strengths.

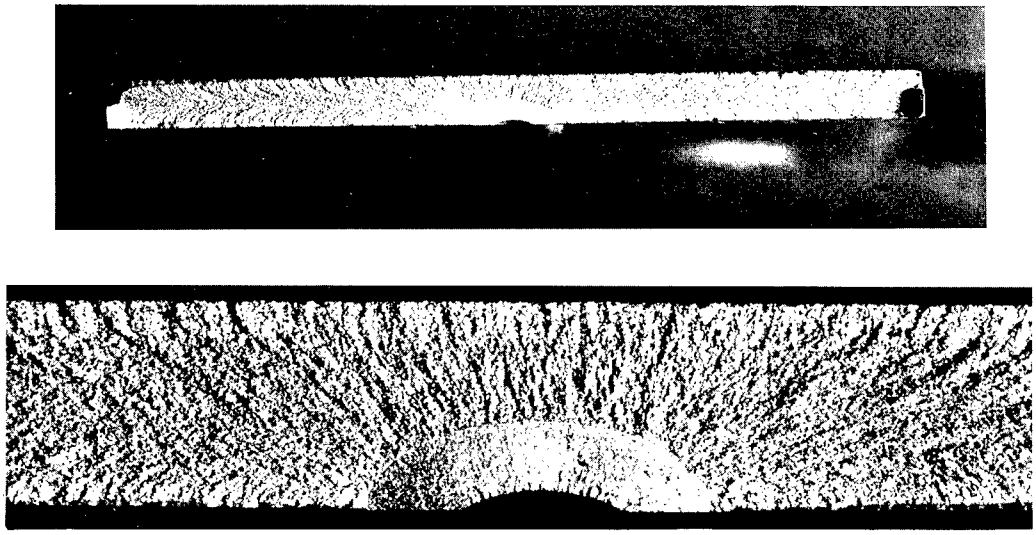

Fig. 3 - Typical fracture of a 8 × 1 × 1/16-inch specimen. Top: entire fracture; bottom: enlarged view of fatigue crack. Dimensions shown in top photo are 1 inch and 1/16 inch.

During fatigue cracking the crack lengths were measured at intervals with a low-power microscope equipped with a micrometer eyepiece. Figure 4 shows the dependence of crack length on the number of cycles for each of the three sets of specimens. This dependence varied among the ten specimens of a given set, and Fig. 4 shows the range of values for each set. It is clear that the rate of crack propagation depends strongly on the maximum deflection, the average crack length increase per thousand cycles being 0.0010, 0.0026, and 0.0142 inch in order of increasing deflection.

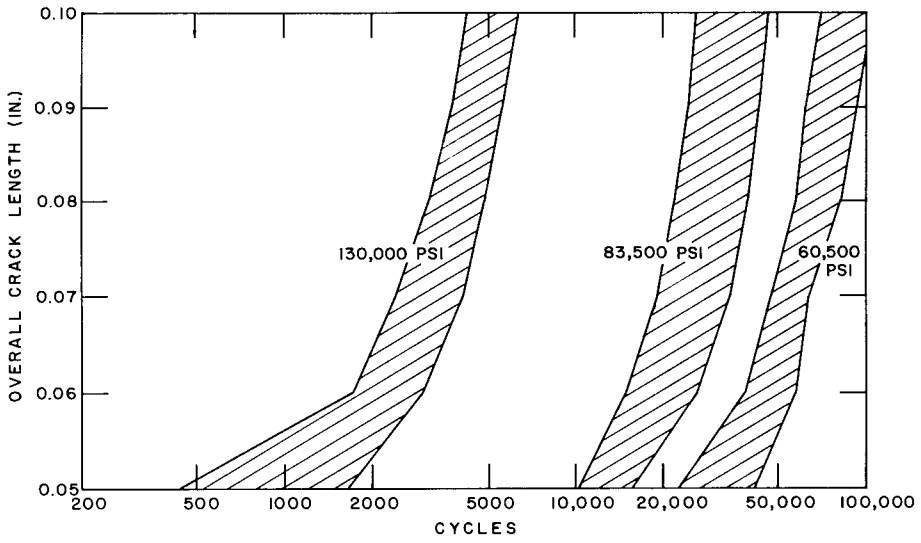

Fig. 4 - Semilog plot of overall crack length vs number of cycles at which the specimen was fatigued to the maximum nominal stress shown. Each band represents the range of values for the ten specimens fatigued at that stress level.

RESULTS AND DISCUSSION

The fatigue-cracked specimens were tested in tension at room temperature (75 to 80°F) in the laboratory atmosphere. The lengths and depths of the fatigue cracks were then measured with a traveling microscope. These dimensions and the gross fracture strengths of the specimens are given in Table 1. Values of the stress intensity factor K were calculated from these data in the manner described in a previous publication (4) and are also given in Table 1.

No evidence was found of slow crack growth occurring at a load appreciably less than the maximum load in any of the tests. A crystal pickup was attached to each specimen during the tests, but no noise indicative of crack extension was heard. Furthermore, close scrutiny of the fracture surfaces failed to reveal any singularities of fracture markings which might indicate slow crack extension (see Fig. 3 for instance). Thus, it is considered that the K values in Table 1 correspond closely to K_{Ic} plane-strain crack toughness values (2,3,4).

Averages and standard deviations of the K values for each group of ten specimens are shown in Table 1. The averages do not differ significantly, but the standard deviation for the group fatigued at 60,500 psi is significantly lower than those for the groups fatigued at higher stresses. The ratio of sample variances is greater than would occur by chance once in twenty times.

Examination of the results showed that the relationship between the K values and the crack dimensions was quite random, whereas there was a strong correlation between the K values and the gross fracture stresses, as shown in Fig. 5. There are three factors which might contribute to the variability of the fracture stress and K: variability of material toughness from specimen to specimen, variability among the fatigue cracks, and possible variable environmental influences during the tests. The third factor can probably be discounted since the tests were all conducted under the same conditions and lasted only a few minutes. It is likely that material toughness variability accounts for some of the variation in the results, but it is also considered likely that variability among the fatigue cracks is the major factor, on account of the significant difference in stress-intensity-factor standard deviations.

Additional specimens were fatigued and then sectioned through the cracks for metallographic examination. No obvious differences could be found between cracks formed at low or high fatigue stresses, the cracks in both cases being very fine with tips beyond the limit of resolution of the optical microscope. The question of possible differences in the fine structure of the material in the immediate vicinity of the crack tips had to remain unresolved because previous experience with replication electron microscopy of the material had shown that this method would be inadequate. It is possible that information might be obtained by transmission electron microscopy, but the problems of preparation of a suitable "thin-film" specimen are formidable.

Apart from the possibility of fine structure differences due to the difference in fatigue stress levels, there is also a strong possibility of a difference in residual stresses. The residual stress around the tip of a fatigue crack might vary from specimen to specimen and might be expected to show greater variation the higher the fatigue stress level. A test of this hypothesis could be made by fatigue cracking specimens before they were heat treated. Presumably any residual stresses from fatigue cracking would be relieved during the heat treatment, and any due to heat treatment should be less variable.

Table 1
Results of Tensile Tests on Fatique-Cracked Specimens

Crack Length (in.)	Crack Depth (in.)	Gross Fracture Stress (psi)	K (psi-in.$^{1/2}$)
60,500 psi*			
0.1050	0.0300	154,000	42,800
0.1040	0.0280	159,700	43,700
0.1010	0.2950	159,500	43,800
0.1010	0.2900	165,000	45,300
0.1010	0.2800	168,500	45,900
0.1040	0.0270	161,000	43,800
0.1050	0.0280	165,000	46,600
0.1030	0.0280	161,700	44,200
0.1020	0.0270	158,200	42,800
0.1010	0.0270	170,500	46,000
Average K: 44,550 Standard Deviation: 1,350			
83,500 psi*			
0.0995	0.0265	177,300	48,000
0.1015	0.0275	167,500	45,600
0.1015	0.0272	153,500	41,400
0.1024	0.0277	159,800	43,500
0.1004	0.0268	170,500	46,200
0.0994	0.0268	148,500	39,500
0.1006	0.0279	162,000	44,100
0.1000	0.0270	145,800	38,800
0.1020	0.0271	170,000	46,400
0.1000	0.0274	169,500	46,200
Average K: 43,950 Standard Deviation: 2,960			
130,000 psi*			
0.1034	0.0300	170,000	47,400
0.1080	0.0318	164,000	46,600
0.1038	0.0298	152,000	41,900
0.1006	0.0295	158,000	43,300
0.1002	0.0291	160,000	44,000
0.1012	0.0291	154,500	42,100
0.1022	0.0299	159,000	43,800
0.1022	0.0288	144,000	39,200
0.1022	0.0289	157,800	43,000
0.1020	0.0289	173,800	47,800
Average K: 43,930 Standard Deviation: 2,580			

*Nominal fatigue stress level.

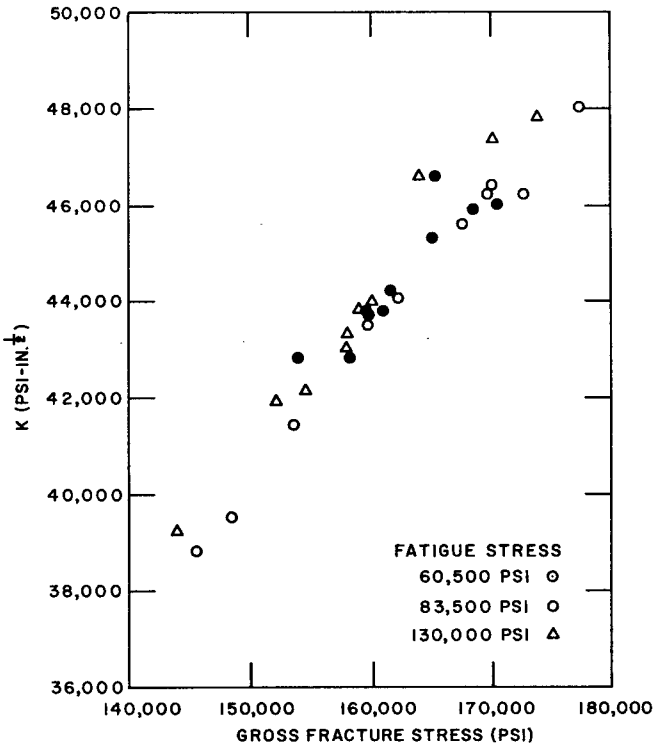

Fig. 5 - Plot of stress intensity factor K vs gross fracture stress for the three groups of specimens indicated by the values of fatigue stress

CONCLUSIONS

Fatigue stressing in bending is a convenient and dependable means of introducing small surface cracks of approximately semielliptical shape into sheet or plate specimens. Plane-strain crack toughness values K can be calculated from the results of fracture tests of such specimens by using a relationship due to Irwin (5). The average K values for groups of ten specimens were found to be independent of the fatigue stressing level, but the standard deviation was found to be significantly lower for the lowest stress level used than for higher stress levels. It is considered that this difference is attributable to factors associated with the fatigue cracks which depend upon the fatigue stress level. Two possibilities are residual stresses and the fine structure of the material in the vicinity of the crack tip.

The results indicate that the nominal fatigue stress level at which a crack is formed may have only a very small effect on the result of a subsequent fracture toughness test, but that the results are likely to be most consistent when cracks are formed at stress levels which are as low as can conveniently be used.

REFERENCES

1. "Fracture Testing of High Strength Sheet Materials: A Report of a Special ASTM Committee," ASTM Bulletin, No. 243, Jan. 1960, p. 29, and No. 244, Feb. 1960, p. 18

2. "Slow Grouth and Rapid Propagation of Cracks: Second Report of a Special ASTM Committee," Materials Research and Standards, 1(No. 5):389, May 1961

3. Irwin, G.R., and Srawley, J.E., "Progress in the Development of Crack Toughness Fracture Tests," Materialprüfung 4:1, Jan 1962

4. Srawley, J.E. and Beachem, C.D., "Fracture of High Strength Sheet Steel Specimens Containing Small Cracks," ASTM Preprint 80a (1961)

5. Irwin, G.R., "Crack Extension Force for a Part-Through Crack in a Plate," to be presented at ASTM Winter Meeting, New York, Nov. 25-30, 1962

6. Yen, C.S., and Pendleberry, S.L., "Technique for Making Shallow Cracks in Sheet Metals," Douglas Aircraft Company Engineering Paper No. 1206, Sept. 1961

7. Srawley, J.E., "Crack Tolerance of AMS 6434 Steel Sheet Stressed Repeatedly," U. S. Naval Research Laboratory Memorandum Report No. 1264 (1962)

APPLICATION OF FRACTURE MECHANICS TO ADHESIVE JOINTS*
[Unclassified]

E. Ripling,† S. Mostovoy,† and R. Patrick‡

The Naval Research Laboratory (Mechanics Division), in anticipation that the performance of the fleet ballistic missile will be materially improved, is exploring, on a long-range basis, the possibilities of developing new materials and design concepts which go substantially beyond those available now for the fleet ballistic missile.

In order to assist our understanding of factors which limit the strength of adhesive bonds, a means for investigating these bonds within the analytical framework of fracture mechanics has been established.

. . . . . FBM Staff

INTRODUCTION

A better understanding of the crack resistance of adhesives is of importance in fiber wound rocket chambers for two reasons. First, there is the obvious need for information about the toughness of large bond areas where nozzles and bosses are attached to the body of the chamber. In addition, since the loads externally applied to the chamber are distributed to the various layers of windings, and indeed to individual fibers by the resin between them, the adhesive toughness is a significant factor in establishing the strength of the structure.

The present project is concerned with evaluating the toughness of adhesives by using the procedures of fracture mechanics. This is a relatively new technique which has met with considerable success when applied to homogeneous systems such as the high-strength steels used for pressure vessels. By the use of fracture mechanics, an intrinsic toughness of the material is measured which makes it possible to determine the load carrying capacity of a structure in the presence of flaws. Thus, minimum toughness standards can be established for the structural materials used in a specific application.

Fracture mechanics has not previously been applied to heterogeneous systems such as adhesive joints. One reason for this is that the difference in elastic moduli of the systems' components makes the mathematical analysis required for calculating stresses in the vicinity of a crack prohibitively difficult. To avoid the need for carrying out these analytical stress analyses, which are available only for single component structures, testing techniques had to be developed that would permit measurement of fracture toughness without knowing the stresses at the crack tip.

Adhesive joints also differ from homogeneous systems in that cracking may occur by a number of different modes. While a metal structure will almost invariably fail due to an opening mode, i.e., from tensile stresses acting normal to the fracture path, adhesive

*Under technical supervision of NRL Code 6210; Contract Nonr 3219 (00) (X).
†Materials Research Laboratory, Inc.
‡Alpha Research and Development, Inc.

joints may also fail due to forward or edgewise shear. Thus, the experimental testing procedure must enable one to evaluate toughness for each of these modes of crack extension as well as the opening mode.

EXPERIMENTAL PROCEDURE

One method that G. R. Irwin has suggested for measuring fracture toughness is the use of a "calibration" bar (1). This procedure has the advantage that it does not require any information about the distribution of stresses at the crack tip. Instead, it measures the total strain energy lost to the system by the propagating crack. The equation for fracture toughness using this procedure is

$$\mathcal{G} = \frac{P^2}{2} \frac{d(1/M)}{da}, \tag{1}$$

where $\mathcal{G}$ = strain-energy release rate, P = applied load over a unit of specimen width, $(1/M)$ = compliance of system, and a = crack length. When P is the critical load required for the crack speed da/dt, then $\mathcal{G}$ from Eq. (1) measures the resistance or critical crack extension force $\mathcal{G}_c$ for the particular speed da/dt. Furthermore, Eq. (1) is applicable to any mode of crack extension. If the applied load acts normal to the fracture path and compliance is measured for this method of loading, the observed fracture toughness is that for an opening mode $\mathcal{G}_{Ic}$. If, on the other hand, P_c is a shear force applied in the direction of crack extension and $(1/M)$ is the corresponding compliance, the fracture toughness measured is that for forward shear $\mathcal{G}_{IIc}$. Evaluating $\mathcal{G}$ by a side shearing mode requires the application of a shear load parallel to the crack front; this measure of fracture toughness is designated $\mathcal{G}_{IIIc}$.

Method for Measuring $\mathcal{G}_{Ic}$

To measure opening mode toughness, a splitting force was applied in the plane of the crack path. This method, rather than the more conventionally used procedure of remote loading, permits control over crack growth. Some preliminary experiments indicated that even with loading in the crack plane, satisfactory control was only obtained when the compliance of the adhesive sample was large. To fulfil these requirements, a double cantilever beam specimen of the type shown in Fig. 1(a) was developed. A schematic diagram of the loading arrangement and a description of the testing procedure are given in Appendix A. The test is carried out by applying a load through fingers that fit into hole F. Prior to collecting data on adhesive systems a master curve of $(1/M)$ versus a, and from this a second curve of $(1/M)$ versus $d(1/M)/da$, was obtained by using a saw-cut solid aluminum sample. With the latter curve it was only necessary to collect data on P_c versus $(1/M)$, as the crack was extended, to calculate $\mathcal{G}_{Ic}$ from Eq. (1).

Method for Measuring $\mathcal{G}_{IIc}$

To find fracture toughness in a forward slipping mode, the specimen in Fig. 1(a) was modified as shown in Fig. 1(b) so that a shear load could be applied to the adhesive. The test piece in this case simply consisted of a tension and a compression member on either side of the glue line so that $d(1/M)/da$ was a constant, and $\mathcal{G}_{II}$ is obtained by multiplying the load for crack extension by a constant which is independent of the crack length a.

Method for Measuring $\mathcal{G}_{Ic}$ and $\mathcal{G}_{IIc}$ Combined

In practice, adhesive systems are subjected to a combination of tension and shear. To evaluate fracture toughness under this loading condition, the $\mathcal{G}_I$ specimen is tilted

on the loading fingers as shown in Fig. 1(c). The tilt angle θ determined the ratio of tensile to shear load developed at the crack tip.

Method for Measuring $\mathcal{G}_{IIIc}$

Although attempts to measure $\mathcal{G}_{IIIc}$ have not yet been made, it is expected that this will present little problem using the specimen shape and loading method shown in Fig. 1(d).

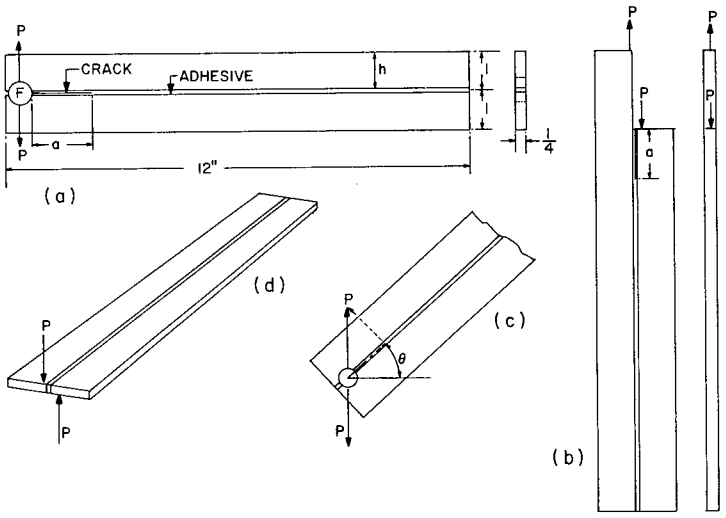

Fig. 1 - Methods of specimen preparation for measuring (a) $\mathcal{G}_I$ (fracture toughness for opening mode), (b) $\mathcal{G}_{II}$ (fracture toughness for forward shear), (c) combined $\mathcal{G}_I$ and $\mathcal{G}_{II}$ (θ determines the ratio of tensile to shear load developed at the crack tip), and (d) $\mathcal{G}_{III}$ (fracture toughness for side shearing mode)

Types of Adhesive and Adherends

Only a single adhesive was studied to date. Because at the initiation of the study it was helpful to locate the crack tip by observing stress fringes, a commercial photostress material, Budd Photostress Type A, was used. The adhesive has an elastic modulus of 0.42×10^6 psi, a tensile strength of 8850 psi and a total elongation of 3.6 percent.

Most of the data collected was on an adhesive system using 2024-T4 aluminum as the adherends. The method of preparing samples from these is given in Appendix B. The glass adherend material was a low-iron crown glass. Its characteristics and method of preparation of samples from it are also given in Appendix B.

TEST RESULTS

Effect of Joint Thickness on $\mathcal{G}_{Ic}$

The first variable to be examined was the effect of joint thickness on $\mathcal{G}_I$ using aluminum adherends, Fig. 2. The data in the top curve were collected on specimens run at a

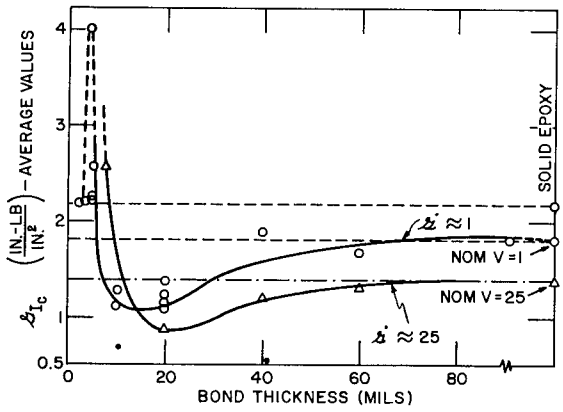

Fig. 2 - Effect of bond (joint) thickness on the critical crack extension force $\mathcal{G}_{Ic}$ for two strain rates. (Each data point is an average of approximately 20 to 30 measurements.)

$d\mathcal{G}/dt$ of about 1 at the instant the crack started to move. This corresponds to a displacement of the loading fingers of approximately 0.01 inch/min.

When the joint was very thick, in the range of 40 to 90 mils, the epoxy in the joint had about the same toughness as the bulk material. Reducing the joint thickness caused a drop in epoxy toughness to a minimum at about 20 mils. A further lowering of the joint thickness caused the toughness to rise abruptly to a maximum that is about twice as high as the toughness of the bulk material. Still thinner joints caused the toughness to drop again. The toughness peak was very narrow, approximately one mil wide. The exact location of the maximum, as well as its width and height, have not been rigorously defined as yet. Indeed, on the basis of the data in Fig. 3, one might question its very existence. However, a rise to about the same level or higher than that of the bulk epoxy is indicated for all thickness below five mils.

The difficulty of defining the exact shape of the $\mathcal{G}_I$ curve results from the difficulty of making specimens whose joint thickness is held constant along the entire specimen length and width and the further problem of measuring this thickness nondestructively. To maintain a sample-making procedure that was as versatile as possible, the specimens were made without the benefit of a jig, and as a consequence there were significant joint thickness variations in all the samples. With thick joints this presented no problems, but in the thinner joints, it obviously was serious.

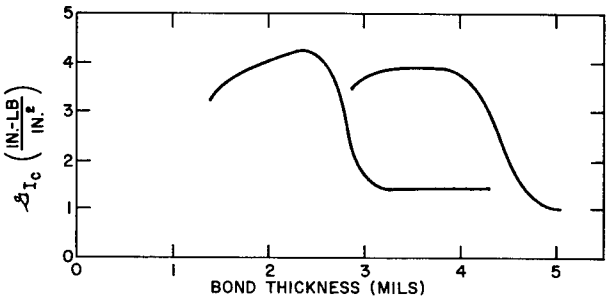

Fig. 3 - $\mathcal{G}_{Ic}$ measured on two specimens with tapered joint thickness varying from 2 to 5 mils along the specimen length

The occurrence of this $\mathcal{G}_I$ peak was verified by using samples in which the joint thickness was purposely tapered. Fracture toughness results obtained on two samples whose glue line nominally varied from 2 to 5 mils along the specimen length are shown in Fig. 3. Although high toughness values over a restricted range of thickness were found in these, the thickness that produces the maximum has still not been ascertained even in the selected specimen shape. Unfortunately even when the location of the peak is established, it is expected to be a function of at least specimen width.

Stability Factor

Although $\mathcal{G}_{Ic}$ is an adequate measure of the energy required for crack motion, two joints with the same toughness may have different fracturing behaviors depending on the geometry of the system. This results because the strain energy in the system is stored in the adherends. As energy is consumed by the advancing crack, a "stiff" system will consume only a small amount of its total energy while a "soft" system will release a significant portion of its energy. Crack growth in the latter then will be far more stable than in the former. In order to quantitatively relate joint configurations with ability to arrest crack propagation, G. Irwin (2) defined the "stability factor" for a stable crack extension tendency as the fractional decrease in $\mathcal{G}$ per unit of crack extension under fixed grip conditions, i.e., as

$$\frac{1}{\mathcal{G}}\frac{d\mathcal{G}}{da}. \tag{2}$$

He suggested that when the stability factor was less than about 0.5 in.$^{-1}$ propagation of cracks takes place uncontrollably. Using this definition, the stability factor has been calculated for specimens with various heights h of adherends (Fig. 4). Note that the specimens become increasingly stable as h is decreased. This chart would indicate that a 3-inch-high specimen has about the same stability with a 6-1/2-inch crack as a 1/2-inch sample has with an 8-inch crack. Although no experimental data are available to support these curves, the behavior is generally consistent with the authors' experience in developing the test sample shape.

The crack length at which control could no longer be exercised over crack growth was noted for the specimens used to get the effect of joint thickness on $\mathcal{G}_I$. The results are shown in Fig. 5. This would indicate that the proposed expression for stability factor might better be written as

$$\frac{1}{h}\frac{1}{\mathcal{G}}\frac{d\mathcal{G}}{da}. \tag{3}$$

Expression (3) indicates a hyperbolic relationship between joint thickness and stability factor as defined in Eq. (2). Since the bulk epoxy became unstable with a five-inch-long crack, this seems a reasonable expression for thick joints. The hyperbolic relationship is not evident in thin joints because the crack length at instability exceeds the specimen length.

Effect of Strain Rate

A very slow strain rate was used to collect the data discussed above; however, a few tests have also been run at a faster rate. The effect of the increased strain rate on the fracture toughness of bulk epoxy is shown by the property loss in the solid material on the extreme right in Fig. 2. Again with thick joints, the epoxy when used as an adhesive had

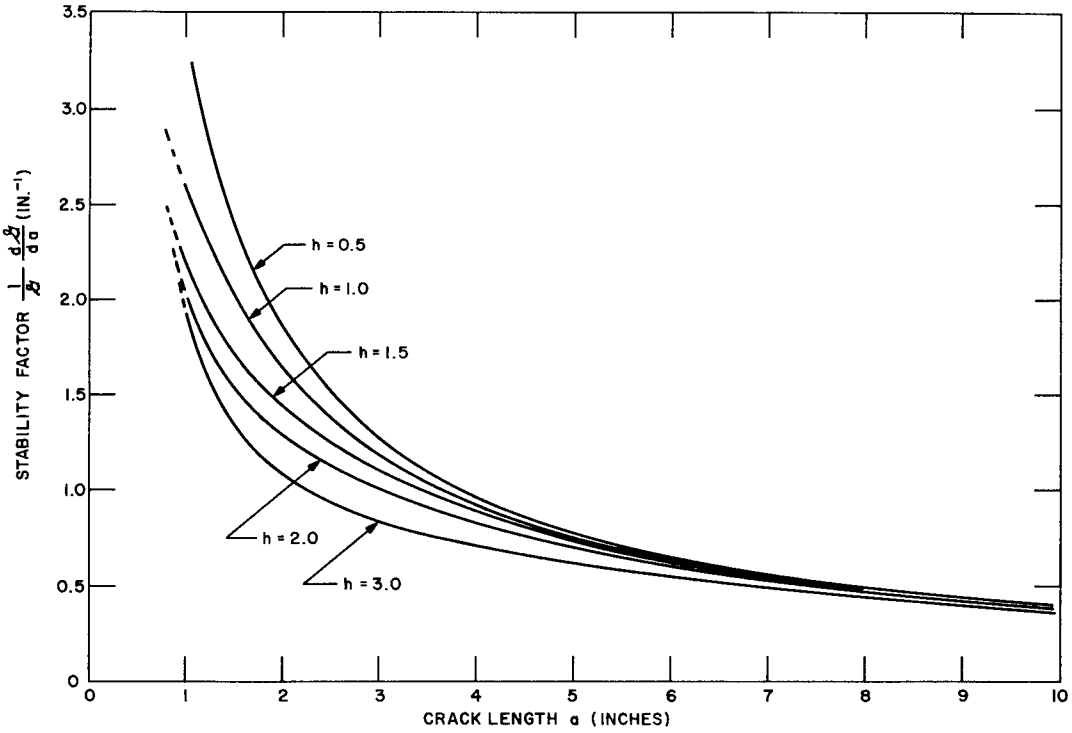

Fig. 4 - Stability factor $1/\mathcal{G}\ d\mathcal{G}/da$ as a function of crack length for specimens of varying height h

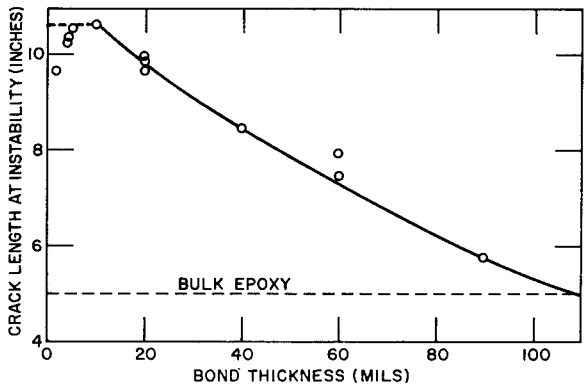

Fig. 5 - Dependence of crack instability on joint thickness

the same toughness as the bulk material, and the strain rate effect appeared to be independent of joint thickness down to about 20 mils. Sufficient tests have not yet been run to describe the effect of strain rate on thinner joints.

Effect of Joint Thickness on G_{IIc}

In a limited number of tests, G_{IIc} was measured on samples of varying joint thickness. The data, shown by circles in Fig. 6, are not sufficiently complete to define the effect of joint thickness on G_{II}, but in all cases the joint is at least an order of magnitude tougher in shear than in tension. The slow strain curve of Fig. 2 is added to this chart for comparison.

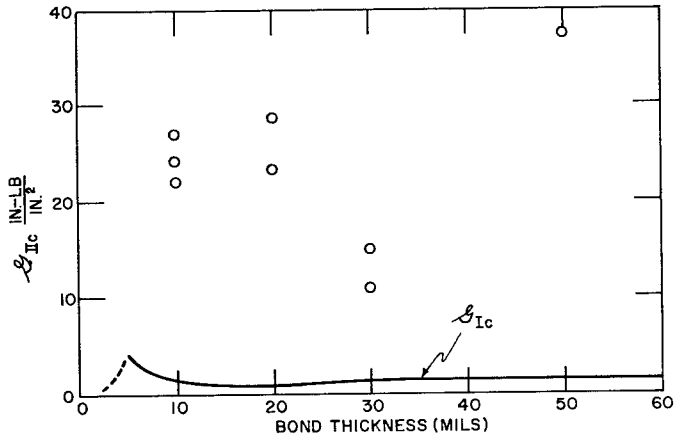

Fig. 6 - Effect of joint thickness on G_{IIc} (circles). The values of G_{Ic} from Fig. 2 are shown for comparison.

Effect of Combined Tension and Shear on G_{Ic}

A few preliminary measurements of G_I with a shear load superimposed onto the tensile load were also made. In all cases the angle of tilt θ, shown in Fig. 1, was 45 degrees so that identical shear and tensile loads were developed at the crack tip. Surprisingly, the addition of the shear component onto the tensile load results in an appreciable increase in opening mode joint toughness, as shown in Table 1.

Table 1
Effect of a Superimposed Shear Load on G_{Ic}

Joint Thickness (mils)	Ratio of Shear Load to Tensile Load	Strain Rate $\dot{G}_{Ic}$	G_{Ic}
20	0	1	1.3 (avg)
20	1	1	4.6
10	0	25	0.8 (avg)
10	1	25	1.7

Effect of Adherend

The results described above were all obtained on an aluminum-epoxy-aluminum system. Since aluminum and glass have the same elastic modulus, bonds made with aluminum and glass adherends would be expected to have the same toughness as long as identical adhesive and joint configuration are used. On testing glass-epoxy-glass, however, $\mathcal{G}_{Ic}$ values were obtained that were far lower than those found with aluminum adherends (Table 2). These lower values of toughness could be traced to poor adhesion of the selected epoxy to the glass as compared with its adhesion to aluminum. When a water drop was placed on opposing fracture surfaces of the aluminum samples, the two contact angles were the same (approximately 60 degrees). On the other hand, the contact angles measured on the glass adherend fracture surfaces were quite different (35 to 40 degrees on one surface and 60 degrees on the other). Initially, organic cleaning was used on the glass. Acid cleaning was found to lower the toughness while flame cleaning improved it. Even with the latter, the toughness of the bonds using glass adherends was only about one-third that of the joints made with aluminum.

The cleaning procedures used on both the aluminum and glass samples is given in Appendix B. In addition to the difference in cleaning method used on the two adherends, the bonded aluminum surface was considerably rougher than the glass, as described in Appendix B.

Table 2
Comparison of Toughness Obtained on Aluminum-Epoxy-Aluminum and Glass-Epoxy-Glass Systems ($\dot{\mathcal{G}}_{Ic}$ = 25)

Adherend	Joint Thickness (mils)	Method of Surface Cleaning	$\mathcal{G}_{Ic}$
Aluminum	10	acid	1.4
	5	acid	2.5
Glass	10	organic	0.33
	10	acid	0.24
	10	flame	0.47
	5	organic	0.23

Fracture Appearance

The appearance of the fracture surface depended on the type of adherend, the joint thickness, and the stress state under which the specimen was fractured. Thick bonds, using aluminum adherends cracked by an opening mode, invariably fractured in the middle of the epoxy layer. The fracture surface was smooth, only interrupted by a number of finger-nail markings along the specimen length, presumably at crack arrest position. As the bonds were made thinner, the fracture surface generally was rougher. The glass samples, on the other hand, always broke near one interface, with a completely smooth surface having no interruptions.

A distinctive crack pattern was formed in the aluminum samples broken by forward shear. The fracture was close to one interface in these samples and a series of 45-degree

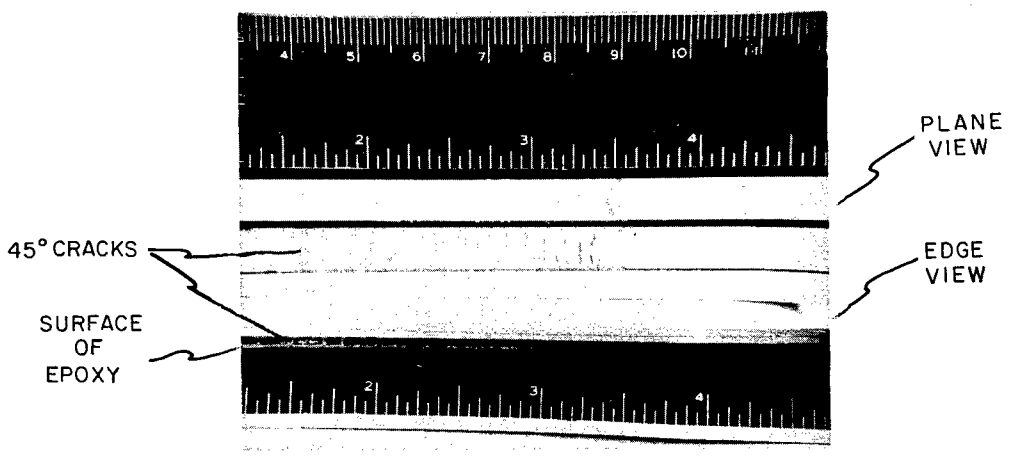

Fig. 7 - Typical appearance of a G_{II} specimen

cracks formed in the epoxy, indicating that the failure was the result of a normal tensile stress. The typical appearance of a G_{II} specimen is shown in Fig. 7.

REFERENCES

1. Irwin, G.R., "Fracture Mechanics," in Structural Mechanics, New York:Pergamon, pp. 557-594, 1960

2. Irwin, G.R., "Application of Fracture Mechanics to Adhesive Joints," Polaris Filament Winding Research Conference, Palo Alto, Calif., Jan. 9-10, 1962

APPENDIX A

METHOD FOR COLLECTING $\mathcal{G}_{Ic}$ AND $\mathcal{G}_{IIc}$ DATA

A schematic drawing of the device used for collecting the data required for $\mathcal{G}_{Ic}$ calculations is shown in Fig. A1. A linear variable differential transformer is mounted on the specimen near the loading holes, after which the specimen is placed on the calibrated loading fingers and the transducer is calibrated with shims for accuracy of vertical displacement. Using a rectified variable dc power supply, the drive motor is activated by applying a voltage corresponding to a given strain rate that has been previously determined. The outputs of both the strain gage load cell and the transducer are recorded simultaneously on an x-y recorder with its ranges set for best determination of slope and critical load for a given crack length.

A microscope and polarized light source are also mounted such that the crack can be observed and its length measured. Because it is difficult to accurately determine the exact location of the crack tip, the observed crack lengths are not used in calculating $\mathcal{G}_{Ic}$. Instead, a calculated crack length determined from the calibrated compliance of the system is used.

If the crack is controllable and the loading rate sufficiently slow, the crack is allowed to run for about 1/4 inch between measurements. Once the crack has run a short distance, the motor is electrically reversed until the specimen is unloaded. This procedure is

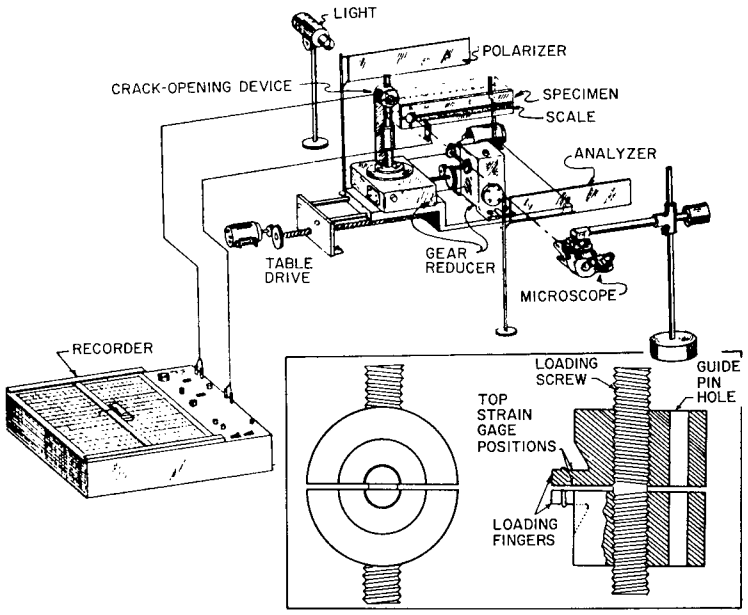

Fig. A1 - Schematic of tensile loading arrangement with enlarged, detailed view of the split circular membrane (crack-opening device)

repeated approximately 20 to 30 times for a single specimen until the crack becomes unstable. The critical loads and slopes, as well as crack length at instability, are logged for $\mathcal{G}_{Ic}$ calculations.

An identical procedure is used for collecting $\mathcal{G}_{Ic}$ data with a superimposed shear load.

When the crack is propagated by forward shear, the test specimen consists simply of one tension and one compression member. Thus the calculated value of $d(1/M)/da$ is a constant and the evaluation of $\mathcal{G}_{IIc}$ only requires measurement of the load at which the crack runs. Because the adhesive is so tough in shear as compared with tension, it was necessary to use a hydraulic tensile machine in a range capable of 5000 pounds for collecting these data. The load is applied by gripping one-half of the specimen in the V-grips of the machine and applying a compressive load to the other half of the specimen by means of a yoke.

APPENDIX B

CLEANING PROCEDURE FOR ALUMINUM AND GLASS SAMPLES

Method of Preparing Aluminum Samples

The aluminum plates used as adherends are milled and ground on the 12 × 1/4-inch face with an open wheel, after which the pieces are cleaned as follows:

1. Degrease in trichloroethylene
2. Vapor degrease with trichloroethylene
3. Treat the metal part by immersion for 10-12 minutes at 150°-170°F in an etching solution consisting of:
   a. Sodium dichromate, $Na_2Cr_2O_7 \cdot 2H_2O$ . . . . . 200 pbw
   b. Sulfuric Acid (sp. gr. 1.84) . . . . . 700 pbw
   c. Distilled Water . . . . . 1700 pbw
4. Rinse thoroughly in cold tap water
5. Final rinse in distilled water
6. Dry in forced-draft oven; the metal temperature should not exceed 140°-150°F

Two of these cleaned pieces are placed on a leveling plate, and the surfaces to be bonded are separated by a shim of the required joint thickness placed at the two ends of the gap. A plug is placed into the loading hole and Teflon tape is pressed over the length of the gap between the plates to form a dam for accepting the epoxy. The assembly is then placed on a hot plate at 150°F and held for 45 minutes to attain equilibrium.

The epoxide components are individually warmed to 105°F and, just prior to pouring, the two components are thoroughly mixed and the temperature of the mixture brought to 105°F. The bond is filled by pouring through a polyethylene funnel having a 1/32-inch orifice. Pouring started at the plugged loading hole and the funnel is drawn along the length of the sample at a speed such that the adhesive overflows the bond and maintains a bank of adhesive in front of the tip. This procedure avoids air entrapment and results in bubble-free samples.

Method of Preparing Glass Samples

The mating surfaces of the glass adherends were ground to seven wavelengths of light. Table B1 summarizes the properties of the glass.

Table B1
Properties of Low-Iron Crown Glass

$\eta_D^{20} = 1.523$; V = 58.8 (dispersion)
Coeff. of Expansion = 9.4×10^{-6}/°C (25°-300°C range)
Softening Point = 1343°C
Color Free Transmission = A/88% illuminant at 0.5 in. thick

The three alternate cleaning procedures used were (a) organic cleaning, (b) acid cleaning, and (c) flame cleaning. These procedures are summarized in Table B2.

Table B2
Methods for Preparing Glass

I.	a. Wash thoroughly with detergent solution b. Dry with hot air gun c. Wash with triply distilled benzene
II.	a. Wash thoroughly with detergent solution b. Dry and place in mixture of sulfuric acid (90)/nitric acid (10) for 30 minutes c. Rinse thoroughly with distilled water d. Dry with hot air gun
III.	a. Wash thoroughly with detergent solution b. Dry with hot air gun c. Wipe off with benzene d. Gently flame with an oxidizing flame

The samples are prepared immediately prior to assembling in order that the surfaces will not become contaminated. Within 30 minutes of cleaning, the glass-epoxy-glass specimens were poured and cured.

A NEW SUBMARINE DETECTION SYSTEM
[Unclassified Title]

A NEW SYSTEM FOR DETECTION OF RADIOACTIVITY INDUCED IN NUCLEAR SUBMARINE WAKES
[[redacted] Title]

G. A. Burginyon, J. W. Butler, and W. H. Jones

The Naval Research Laboratory (Nucleonics Division) is presently engaged in a program to increase the knowledge of the environment in which a submarine operates and to develop a method of obtaining information pertaining to the influence of the submarine on this environment.

Previous efforts toward the detection of the radioactivity left in the wake of a nuclear-powered submarine have involved the use of simple ungated Geiger counters or ungated scintillation detectors. The system described herein utilizes a time-coincidence scheme to reduce normal background with respect to the counting rate expected from the residual radioactive isotopes sodium-24 and chlorine-38 from the wake of the nuclear-powered submarine.

. . . . . FBM Staff

INTRODUCTION

The reactor in a nuclear submarine is a prolific source of neutrons, some of which penetrate the hull and enter the surrounding water. The great majority of these neutrons are captured by elements of the sea water which lead to no, or very weak, radioactivity. However, a small fraction of the neutrons is captured by sodium nuclei producing Na^{24} which has a half-life of about 15 hours. Another small fraction of the neutrons is captured by some of the chlorine nuclei producing Cl^{38}, which has a half-life of about 37 minutes. The research to be described involves the detection, by means of radiation-sensitive instruments, of the Na^{24} and Cl^{38} isotopes in the wake of a nuclear-powered submarine.

The concept of detecting the radioactive trail of a nuclear submarine is not new. The original specifications for nuclear submarines included a maximum permissible neutron leakage, calculated to make the radioactivity of sodium in the wake small compared with the natural radiations in the sea, mainly from K^{40}, so that it would be essentially impossible to detect the wake. A number of subsequent independent studies have also shown that the detection of the radioactive trail is indeed impossible with conventional techniques.

The system to be described differs from conventional systems by taking advantage of a particular characteristic of Na^{24} and Cl^{38} which enables one to differentiate them from the much more intense natural radiation in the sea water. The characteristic referred to is that both Na^{24} and Cl^{38} emit two gamma rays simultaneously when one such nucleus decays, whereas the radioactive atoms naturally occurring in sea water, for example K^{40}, emit only one gamma ray for each decay. Thus, by having two independent detectors of gamma rays and by recording only those events when both detectors count at the same instant, one can virtually eliminate the background due to K^{40} and most other natural radioactive atoms in sea water. The detection of a radioactive trail, which had formerly appeared impossible, now shows promise.

APPARATUS AND PROCEDURE

A water sample is removed from the wake, and the salt is concentrated by evaporation and then placed in a thin rubber container between two detectors, which are sodium iodide (thallium activated) crystals 5 inches in diameter and 6 inches long. A block diagram of the two-dimensional coincidence analyzer is shown in Fig. 1. Except for the oscilloscope driver circuits and the scaler, the system is completely transistorized.

There are two crystals with identical parallel circuits detecting gamma rays emitted by the radioactive sample. Let us suppose that a single gamma ray from the sample interacts in crystal y. The 3-inch multiplier phototube (type 6363) optically coupled to the crystal will send a small pulse to the gamma-ray amplifier. Here the pulse is amplified and then fed both to a Schmitt trigger circuit and to a delay line. The delayed pulse is further amplified in the oscilloscope driver circuit to a maximum of 180 volts and applied directly to the vertical deflection plates of the cathode-ray tube (3RP11A). The other amplifier output connects to a Schmitt trigger circuit which emits a constant size and shape pulse for input pulses above a certain fixed amplitude. This pulse is now fed to a fast coincidence circuit, consisting of biased diodes, which will produce no output pulse when only a single input pulse is applied. Since the output from the fast coincidence circuit is used to turn on the beam of the cathode-ray tube (which is normally turned off), no trace can occur on the oscilloscope for a single event in either crystal. If, however, two pulses, one from each of the two crystals, arrive at the fast coincidence circuit within 0.1 microsecond of each other, the circuit will be activated and a pulse will be sent to the

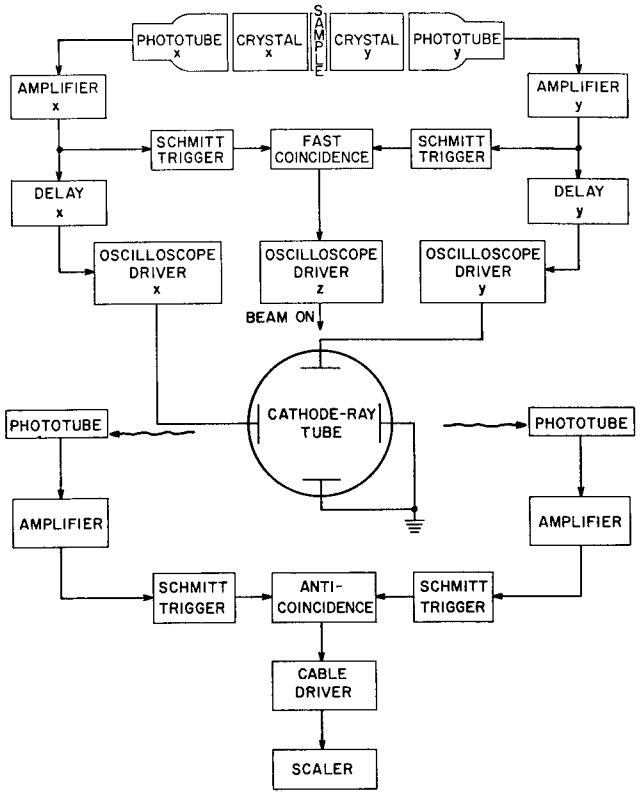

Fig. 1 - Block diagram of the coincidence-anticoincidence electronic detector system

oscilloscope driver circuit. Here the pulse is effectively amplified and shaped and then used to turn on the beam of the cathode-ray tube. Thus if two gamma rays interact simultaneously in the two crystals, one gamma ray in crystal y and one gamma ray in crystal x, then simultaneous pulses will occur in both halves of the circuit. These pulses will activate the fast coincidence circuit, which turns on the cathode-ray beam, and they will also appear on the deflection plates of the cathode-ray tube, thus producing a trace on the oscilloscope. The voltage on the vertical deflection plates of the oscilloscope is proportional to the energy deposited in crystal y and the voltage on the horizontal deflection plates of the oscilloscope is proportional to the energy deposited in crystal x. It is thus possible to calibrate the ordinate and abscissa of the oscilloscope in Mev. Therefore, for gamma rays which are detected simultaneously, the oscilloscope will show a trace which terminates at the coordinate (E_x, E_y), where E_x corresponds to the energy deposited in crystal x and E_y corresponds to the energy deposited in crystal y.

The double photopeak interaction of the Na^{24} isotope (which results when all the energy of each gamma ray is deposited in its respective crystal) will produce a compact cluster of traces terminating in a small area at coordinate (E_1, E_2) and a similar cluster at coordinate (E_2, E_1), where E_1 and E_2 are the energies of the Na^{24} gamma rays (1). A cluster of traces will also appear at coordinates (E_3, E_4) and (E_4, E_3) caused by the Cl^{38} gamma rays. (See Fig. 2 for a simplified diagram of the decay schemes of Na^{24} and Cl^{38}.) The reason for the two concentrations of traces for each radioactive isotope is that either gamma ray can enter either crystal, resulting in symmetry about a 45-degree line from the origin of the trace provided that the gains in both halves of the circuit are equal.

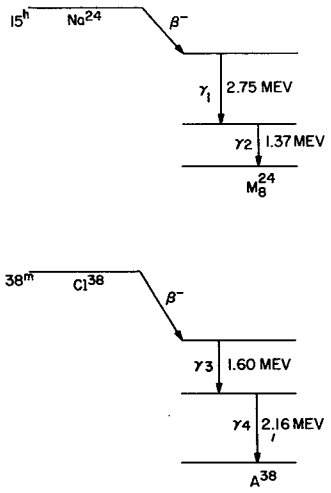

Fig. 2 - A simplified diagram of the decay schemes of the Na^{24} and Cl^{38} isotopes. Only those features in the decay scheme pertinent to the present report are included.

In addition to double photopeak interactions there are Compton-photopeak interactions and Compton-Compton interactions in the two crystals. A Compton interaction usually leads to the situation where only a part of the gamma-ray energy is deposited in the crystal, the rest of the energy leaving the crystal in the form of a lower energy gamma-ray photon. (A schematic diagram of a typical display on the oscilloscope face is shown in Fig. 3. In order to avoid confusion only double photopeak traces are shown in the display.)

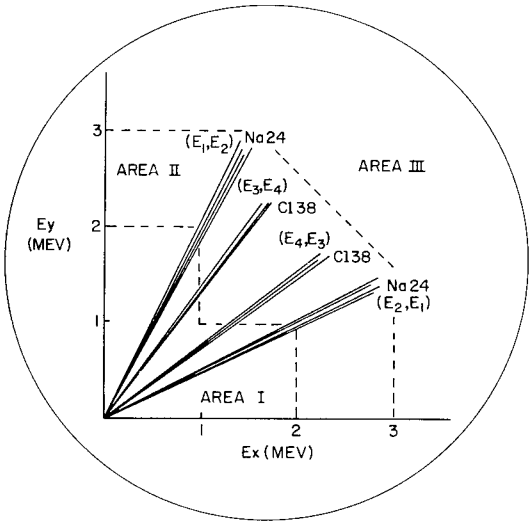

Fig. 3 - Schematic representation of the display produced on the oscilloscope face by the Na^{24} and Cl^{38} isotopes. To avoid confusion only those traces resulting from a double photopeak interaction are shown. The dotted lines enclose the area (Area II) in which most traces caused by Na^{24} and Cl^{38} terminate. About 90 percent of the background traces terminate in Area I. Occasional high-energy background traces will sweep through Area II and terminate in Area III. The coordinate (E_x, E_y) for the two possible locations of the trace cluster for each isotope are also indicated.

The face of the oscilloscope is divided by dotted lines into three regions labeled Area I, II, and III in Fig. 3. About 90 percent of the background traces terminate in Area I, most Na^{24} and Cl^{38} double photopeak and Compton-photopeak traces terminate in Area II, and high-energy background traces due mostly to cosmic-ray muons terminate in Area III.

Two three-quarter-inch phototubes (6365) are optically coupled to Area II by a lucite light pipe. Two additional phototubes are optically coupled to Area III in a similar manner. If a trace terminates in Area II, the phototubes watching this area produce an output pulse. This pulse is amplified and fed to a Schmitt trigger circuit where it is shaped and sent through an anticoincidence circuit. The pulse is now fed to a cable driving circuit and finally to a scaler where a count is recorded. If, however, a trace sweeps through Area II and terminates in Area III, a rejection pulse will be produced by the phototubes watching Area III, in addition to the pulse from Area II which was described above. After amplification followed by shaping in a Schmitt trigger, this rejection pulse is applied to the anticoincidence circuit. While the rejection pulse is present the anticoincidence circuit will not pass the pulses from Area II and thus no count can be registered in the scaler. Therefore, only pulses which terminate in Area II are recorded. Since most Na^{24} and Cl^{38} traces terminate in Area II and only a small fraction of the background traces end in this area, the system is selective with respect to energy.

The energy resolution for double photopeak traces on the oscilloscope face is approximately 1 percent. However, the energy gate at the face of the oscilloscope is widened (Area II enlarged) in order to accept traces produced by photopeak-Compton and Compton-Compton interactions in addition to the double photopeak interactions. This reduces the energy resolution but, at the same time, increases the sensitivity of the system. In the present system the acceptance area (Area II) is approximately 20 percent of the total area within which pulses may terminate.

At the present stage of equipment development it appears desirable, based on calculations of the expected counting rate, to lower the sample and the entire electronic apparatus in a pressure vessel to a depth of several hundred feet in water to greatly reduce background

counting rate from cosmic rays at depth compared to the surface. This reduction in background is due to the shielding effect of the sea water. The background counting rate of the system at depth is 0.04 count per minute.

A multiconductor cable is used to supply power to the equipment in the pressure vessel and to allow a continuous readout of the data on the surface. The scaler is the only piece of equipment shown in Fig. 1 which remains on the surface.

The system is calibrated with the coincidence gamma rays of Na^{24} (2.75 and 1.38 Mev) and Co^{60} (1.33 and 1.17 Mev).

The efficiency of the system for Na^{24} is 0.26 percent. This efficiency is defined as the Na^{24} counting rate in Area II divided by the source strength. The sensitivity of this system is 6.9×10^{-12} curies, which corresponds to a signal-to-noise ratio of one.

EXPERIMENTAL DATA

In June 1960, this detection scheme was tested (2) with a sea-water sample from beneath the Nautilus while it was docked at Portsmouth, New Hampshire. A tidal current of about 2 knots was flowing by the vessel's hull. A hose was attached at the keel directly under the reactor compartment in order to collect the sea-water sample. The reactor was being operated at 50 percent of maximum power. The vacuum-tube prototype system then in use was not portable so the sample was transported to the U.S. Naval Research Laboratory where it was counted. About ten hours elapsed between irradiation and counting. Essentially all of the chlorine had decayed by that time, but the "signature" of the radioactive sodium was clearly visible, about 50 times background.

A new transistorized system was developed in 1961 and field tested at Key West, Florida, in May 1962. During these tests a sample was taken from beneath the Nautilus while it was docked at Key West, Florida. An estimated one-quarter knot current was flowing beneath the Nautilus. The reactor was operating at 10 percent of full power. The 5-gallon sample was concentrated and then counted one hour after extraction from beneath the Nautilus. It was not necessary to lower the pressure vessel as the initial signal-to-noise ratio on the surface was 45.

The signal-to-noise ratio at depth would have been approximately 1000. A simple calculation shows that the combined Na^{24} and Cl^{38} signal would have been detectable on the surface without concentration of the salt with a signal-to-noise ratio greater than two.

In a plot of counting rate versus time the separate contributions of the Cl^{38} and Na^{24} isotopes were easily observed. Detectable pulses from the Cl^{38} isotope persisted for three hours after extraction of the water sample from beneath the Nautilus. The Na^{24} isotope was still detectable after 29 hours with a signal-to-noise ratio of 6 on the surface and 150 at depth.

DISCUSSION

Numerous calculations (1,3) have been made of the radioactivity produced in sea water by passage of a nuclear-powered submarine. Invariably the results of these calculations depend in a sensitive way upon many assumptions, such as: the total neutron leakage in neutrons per second from the submarine's hull, the distribution of radioactivity throughout

the wake, the volume of the wake as a function of time after passage of the submarine, etc. The results of most of these calculations indicate that the present system is probably capable of detecting the nuclear wake shortly after passage of the submarine.

Butler (1) calculates the counting rate produced in a system similar to the present one by a sample removed from the wake of a nuclear submarine. It is now possible to improve the assumptions made by Butler and, in fact, to make the calculation apply to the present system. Using the value recently determined by Miranda et al. (4) for the total neutron leakage from the Nautilus, and making a set of assumptions which approximate the conditions of the Key West measurement, one calculates a theoretical signal-to-noise ratio of five for the Key West measurement. The actual experimental value was approximately 1000, which is 200 times larger than the calculated value. This suggests that the assumptions made in arriving at the calculated value may be too conservative, and that the signal being sought may be more intense than calculations would indicate.

Problems to be solved include the difficulty in successfully extracting a sample from the nuclear wake. The precise size, shape, and depth of the nuclear wake immediately aft of the submarine is unknown. At the present stage of equipment development it is necessary to concentrate the salt in the sample by evaporation and to lower the concentrated sample in a pressure vessel to reduce the background counting rate by a factor of approximately 23. Since these two operations require about one-half hour, one must probe the wake for a sample and later process it without any assurance that the sample was actually extracted from the nuclear wake. The delayed readout of this prototype model of the detector system greatly increases the difficulty in obtaining a sample from the nuclear wake. It is hoped that the sensitivity of future prototype systems will be sufficiently increased so that it will not be necessary to concentrate the sample or lower it in a pressure vessel.

The practical application of this system to the detection of a nuclear wake depends on the spatial distribution of the wake as a function of time. There is some experimental evidence that the nuclear wake remains a well-defined entity for several hours after passage of a submarine (5).

The ability of this system to detect a nuclear-powered submarine is directly dependent on the neutron leakage from this submarine. In the design of this system it has been assumed that the neutron leakage of a potential enemy submarine is the same as from our submarines.

A simple modification in the present system could enable it to count the Cl^{38} and Na^{24} gamma rays separately. From the relative counting rates of the two isotopes one can calculate the elapsed time since passage of the nuclear submarine. This modification has not been made in the present system because the main problem, at present, is detection of the submarine.

Although many problems exist, particularly in successfully extracting a sample from the nuclear wake, these problems do not, at present, appear insurmountable and work is continuing. The next step will involve extracting a sea-water sample from beneath the reactor of a nuclear submarine while it is underway. When this step is successfully concluded, wake-sampling equipment will be developed to be operated from a surface ship, and samples will be taken from the nuclear wake aft of the submarine.

Many improvements can and will be made in this equipment. It is hoped that it will prove to be valuable not only in classifying nuclear submarines, but also in providing a new technique for the study of the diffusion, drifting, and dissipation of wakes.

[redacted]

UNCLASSIFIED

REFERENCES

1. Butler, J.W., "A Novel Submarine Detection System," NRL Report 5410 ([redacted] Report, Unclassified Title), Dec. 9, 1959

2. Butler, J.W., "Preliminary Test of a Novel Submarine Detection System," NRL Report 5571 ([redacted] Report, Unclassified Title), Nov. 15, 1960

3. Lowry, J.W., "Detection of Nuclear Submarines by Induced Radioactivity," Navord Report 6052 ([redacted] Report), Feb. 10, 1958

4. Miranda, H.A., Jr., and Rooney, P.S., "Measurement of Neutron Leakage from the USS Nautilus," Hudson Laboratories TR92 ([redacted] Feb. 26, 1962

5. Miranda, H.A., Jr., Schimmel, H., and Rooney, P.S., "Mass Transport in the Wake of a Submerged Submarine," Hudson Laboratories TR87 ([redacted]), Apr. 6, 1961

[redacted]